

ARTICLE

A TRPA1 inhibitor suppresses neurogenic inflammation and airway contraction for asthma treatment

Alessia Balestrini¹, Victory Joseph², Michelle Dourado³, Rebecca M. Reese³, Shannon D. Shields³, Lionel Rougé⁴, Daniel D. Bravo⁵, Tania Chernov-Rogan⁵, Cary D. Austin⁶, Huifen Chen⁷, Lan Wang⁷, Elisia Villemure⁷, Daniel G.M. Shore⁷, Vishal A. Verma⁷, Baihua Hu⁸, Yong Chen⁸, Laurie Leong⁶, Chris Bjornson⁶, Kathy Hötzel⁶, Alvin Gogineni², Wyne P. Lee⁹, Eric Suto⁹, Xiumin Wu⁹, John Liu⁹, Juan Zhang⁹, Vineela Gandham², Jianyong Wang⁵, Jian Payandeh⁴, Claudio Ciferri⁴, Alberto Estevez⁴, Christopher P. Arthur⁴, Jens Kortmann¹, Ryan L. Wong¹, Jose E. Heredia¹, Jonas Doerr¹⁰, Min Jung¹⁸, Jason A. Vander Heiden¹⁸, Merone Roose-Girma¹⁰, Lucinda Tam¹⁰, Kai H. Barck², Richard A.D. Carano², Han Ting Ding¹¹, Bobby Brillantes¹², Christine Tam¹², Xiaoying Yang¹³, Simon S. Gao¹⁴, Justin Q. Ly¹⁵, Liling Liu¹⁵, Liuxi Chen¹⁵, Bianca M. Liederer¹⁵, Joseph H. Lin¹⁶, Steven Magnuson⁷, Jun Chen⁵, David H. Hackos³, Justin Elstrott², Alexis Rohou⁴, Brian S. Safina⁷, Matthew Volgraf⁷, Rebecca N. Bauer¹⁷, and Lorena Riol-Blanco¹

Despite the development of effective therapies, a substantial proportion of asthmatics continue to have uncontrolled symptoms, airflow limitation, and exacerbations. Transient receptor potential cation channel member A1 (TRPA1) agonists are elevated in human asthmatic airways, and in rodents, TRPA1 is involved in the induction of airway inflammation and hyperreactivity. Here, the discovery and early clinical development of GDC-0334, a highly potent, selective, and orally bioavailable TRPA1 antagonist, is described. GDC-0334 inhibited TRPA1 function on airway smooth muscle and sensory neurons, decreasing edema, dermal blood flow (DBF), cough, and allergic airway inflammation in several preclinical species. In a healthy volunteer Phase 1 study, treatment with GDC-0334 reduced TRPA1 agonist-induced DBF, pain, and itch, demonstrating GDC-0334 target engagement in humans. These data provide therapeutic rationale for evaluating TRPA1 inhibition as a clinical therapy for asthma.

Introduction

Asthma is a chronic respiratory syndrome characterized by variable airflow obstruction, airway hyperresponsiveness (AHR), airway inflammation, and symptoms including cough, breathlessness, and wheezing (Braman, 2006; Cohn et al., 2004; Fahy, 2015; Maddox and Schwartz, 2002). Recent advances led to identification of two major endotypes of asthma based on the level of Type-2 cytokine-driven inflammation: “Type-2 high” and “Type-2 low.” Type-2 high patients exhibit elevated blood and sputum eosinophils, IgE, fractional exhaled nitric oxide,

and Type-2 cytokines (Galli and Tsai, 2012; Staton et al., 2016; Woodruff et al., 2009). Antibody therapies that target Type-2 cytokines or IgE are efficacious at reducing the risk of asthma exacerbations and airflow limitation in Type-2 high patients but have failed to significantly ameliorate symptoms (Corren et al., 2011; Fahy, 2015; Hanania et al., 2013; Ortega et al., 2014; Ortega et al., 2016; Rabe et al., 2018). Additionally, the molecular mechanisms driving asthma in patients with low levels of Type-2 biomarkers remain largely unknown, in

¹Department of Immunology Discovery, Genentech, Inc., South San Francisco, CA; ²Department of Biomedical Imaging, Genentech, Inc., South San Francisco, CA; ³Department of Neuroscience, Genentech, Inc., South San Francisco, CA; ⁴Department of Structural Biology, Genentech, Inc., South San Francisco, CA; ⁵Department of Biochemical and Cellular Pharmacology, Genentech, Inc., South San Francisco, CA; ⁶Department of Pathology, Genentech, Inc., South San Francisco, CA; ⁷Department of Discovery Chemistry, Genentech, Inc., South San Francisco, CA; ⁸Pharmaron-Beijing Co. Ltd., BDA, Beijing, People’s Republic of China; ⁹Department of Translational Immunology, Genentech, Inc., South San Francisco, CA; ¹⁰Department of Molecular Biology, Genentech, Inc., South San Francisco, CA; ¹¹Department of Clinical Pharmacology, Genentech, Inc., South San Francisco, CA; ¹²Department of Biomolecular Resources, Genentech, Inc., South San Francisco, CA; ¹³Department of Product Development Biometric Biostatistics, Genentech, Inc., South San Francisco, CA; ¹⁴Department of Clinical Imaging, Genentech, Inc., South San Francisco, CA; ¹⁵Department of Drug Metabolism and Pharmacokinetics, Genentech, Inc., South San Francisco, CA; ¹⁶Department of Early Clinical Development, Genentech, Inc., South San Francisco, CA; ¹⁷Department of OMNI-Biomarker Development, Genentech, Inc., South San Francisco, CA; ¹⁸Department of OMNI Bioinformatics, Genentech, Inc., South San Francisco, CA.

Correspondence to Lorena Riol-Blanco: riol-blanco.lorena@gene.com; Rebecca N. Bauer: bauer.rebecca@gene.com.

© 2021 Genentech. This article is distributed under the terms of an Attribution–Noncommercial–Share Alike–No Mirror Sites license for the first six months after the publication date (see <http://www.rupress.org/terms/>). After six months it is available under a Creative Commons License (Attribution–Noncommercial–Share Alike 4.0 International license, as described at <https://creativecommons.org/licenses/by-nc-sa/4.0/>).

part due to lack of preclinical models that recapitulate this endotype. Thus, an approach that combines multiple preclinical models of relevant asthma traits is necessary to identify novel mechanisms and evaluate potential therapeutics for asthma.

Communication between local sensory neurons, immune cells, and resident lung stromal cells appear to be key drivers of AHR, airway obstruction, and inflammation (Canning et al., 2014; Drake et al., 2018; Ordovas-Montanes et al., 2015). Activation of sensory neurons by exogenous irritants or endogenous inflammatory mediators results in neuropeptide release in the airways, as well as signaling to the central nervous system to initiate an “urge to cough,” breathing pattern changes, and dyspnea (Burki and Lee, 2010). Asthmatics have heightened cough reflex sensitivity, suggesting that the airway sensory neurons of asthmatics may exist in a hypersensitive state (Drake et al., 2018; Koskela et al., 2004; Koskela et al., 2008; Satia et al., 2017; Satia et al., 2019). Hence, there is mounting evidence that targeting neuronal inputs could be a therapeutic strategy to alleviate asthma symptoms (Belvisi et al., 2016).

Lungs are predominantly innervated by vagal sensory neurons that are activated by mechanical and chemical stimuli (Chang et al., 2015). Noxious stimuli are detected by an array of receptors expressed by a subpopulation of neurons called nociceptors that sense environmental and internal signals to regulate bronchoconstriction, breathing patterns, vasodilatation, mucus production, and inflammation (Mazzone and Udem, 2016). One of the most versatile of these receptors is transient receptor potential (TRP) cation channel member A1 (TRPA1; Hondoh et al., 2010; Nassenstein et al., 2008). TRPA1 is a nonselective cation channel that acts as a chemosensor for many exogenous irritants and endogenous ligands including proinflammatory mediators (Andr e et al., 2008; Bautista et al., 2013; Bessac et al., 2009; Bessac et al., 2008; Viana, 2016). Several endogenous TRPA1 activators are elevated in the airways of asthmatics (Grace et al., 2014; Maher et al., 2011). In humans, TRPA1 polymorphisms correlate with reduced asthma control (Gallo et al., 2017). TRPA1 in human lungs is also expressed by nonneuronal cells with known contributions to asthma, including airway smooth muscle (ASM) and fibroblasts (Belvisi and Birrell, 2017; Virk et al., 2019). Genetic deletion or pharmacologic inhibition of TRPA1 diminishes airway inflammation and AHR in mouse and rat models (Caceres et al., 2009; Devos et al., 2016; Hox et al., 2013; Reese et al., 2020). In humans, activation of TRPA1 in vagal sensory afferents leads to changes in breathing pattern, dyspnea, and cough (Belvisi et al., 2016).

Despite great interest in targeting TRPA1, development of a TRPA1 inhibitor with optimal in vivo characteristics has been challenging (Chen and Hackos, 2015; Moran, 2018; Skerratt, 2017). Multiple mechanisms of action by which TRPA1 might contribute to asthma and varying TRPA1 expression patterns across preclinical species have complicated the validation path for TRPA1 inhibitors under evaluation for use in human trials (Bianchi et al., 2012; Klionsky et al., 2007; Nagatomo and Kubo, 2008).

Here, we report the identification of GDC-0334, a highly potent, selective, and orally bioavailable small molecule inhibitor (SMI) of TRPA1 with pharmacologic activity conserved

across four species in vivo. By combining genetic and pharmacologic approaches in several preclinical models, these results clarify the contribution of TRPA1 expressed by vagal sensory neurons and ASM to airway inflammation, edema, and cough. Moreover, GDC-0334 dose proportionally modulated pharmacologic activity in a Phase 1 study of healthy volunteers.

Results

Functional activity of neuronal and nonneuronal TRPA1 in the lungs across species

Expression of TRPA1 in trigeminal, vagal, and dorsal root ganglia (DRGs) sensory neurons was previously established (Jordt et al., 2004; Reese et al., 2020; Rostock et al., 2018; Story et al., 2003; Yu and Ouyang, 2009). However, questions remain regarding TRPA1 expression and function in lung resident nonneuronal cells (Virk et al., 2019). In this regard, TRPA1 gene expression and functional activity were compared across several lung cell types and species. TRPA1 mRNA was detected in primary human lung fibroblasts (HLFs) and human ASM cells (HASMCS), but not human airway epithelial cells (HAECs) and lung endothelial cells (Fig. S1 A). TRPA1 mRNA levels tracked with calcium flux responses after treatment of human primary cells with the TRPA1 agonist AITC, confirming the presence of functional TRPA1 in HASMCs and HLFs, but not HAECs (Fig. 1 A, black bars; Fig. 1 B; Fig. S1, B and D, black bars of the bar chart; and Fig. S1 C). *Trpa1* expression was found in DRGs from all preclinical species investigated (Fig. 1 C and Fig. S1 E). However, unlike in humans, no expression of *Trpa1* was detected in nonneuronal lung cells in preclinical species with the exception of guinea pig ASM (Fig. 1 C and Fig. S1, E and G). TRPA1 agonist-induced calcium flux in guinea pig ASM cells demonstrated the presence of functional TRPA1 and highlighted the utility of this species in the study of TRPA1-related ASM physiology (Fig. 1 B and Fig. S1 G).

To elucidate the contribution of neuronal and nonneuronal sources of TRPA1 in vivo, we used the OVA challenge model of asthma in mice, as genetic deletion of TRPA1 was previously shown to reduce allergic airway inflammation in this model (Caceres et al., 2009; Reese et al., 2020). TRPA1 is expressed by a population of sensory neurons called nociceptors that are characterized by the presence of the voltage-gated sodium channel Nav1.8 (encoded by the *Scn10a* gene; Baral et al., 2018; Chen and Hackos, 2015; Hjerling-Leffler et al., 2007; Riol-Blanco et al., 2014). Depletion of Nav1.8⁺ nociceptors abolished TRPA1 expression in sensory ganglia (Fig. S2 A). Then, *Scn10a-Dtr⁺* and *Scn10a-Dtr⁻* control mice were OVA sensitized, and after 21 d, Nav1.8⁺ nociceptors were deleted upon diphtheria toxin (DT) treatment. Both groups were subsequently challenged or not with aerosolized OVA for 7 d (Fig. S2 B). The resulting bronchoalveolar lavage fluid (BALF) infiltrates were reduced by ~50% in *Scn10a-Dtr⁺* mice compared with *Scn10a-Dtr⁻* control mice (Fig. 1 D and Fig. S2 C), confirming the contribution of nociceptors to airway inflammation (Talbot et al., 2015). A similar decrease was observed in *Trpa1^{-/-}* mice compared with *Trpa1^{+/+}* littermates (Fig. 1 E and Fig. S2 C, right), suggesting that TRPA1 may modulate airway inflammation through a neurogenic mechanism.

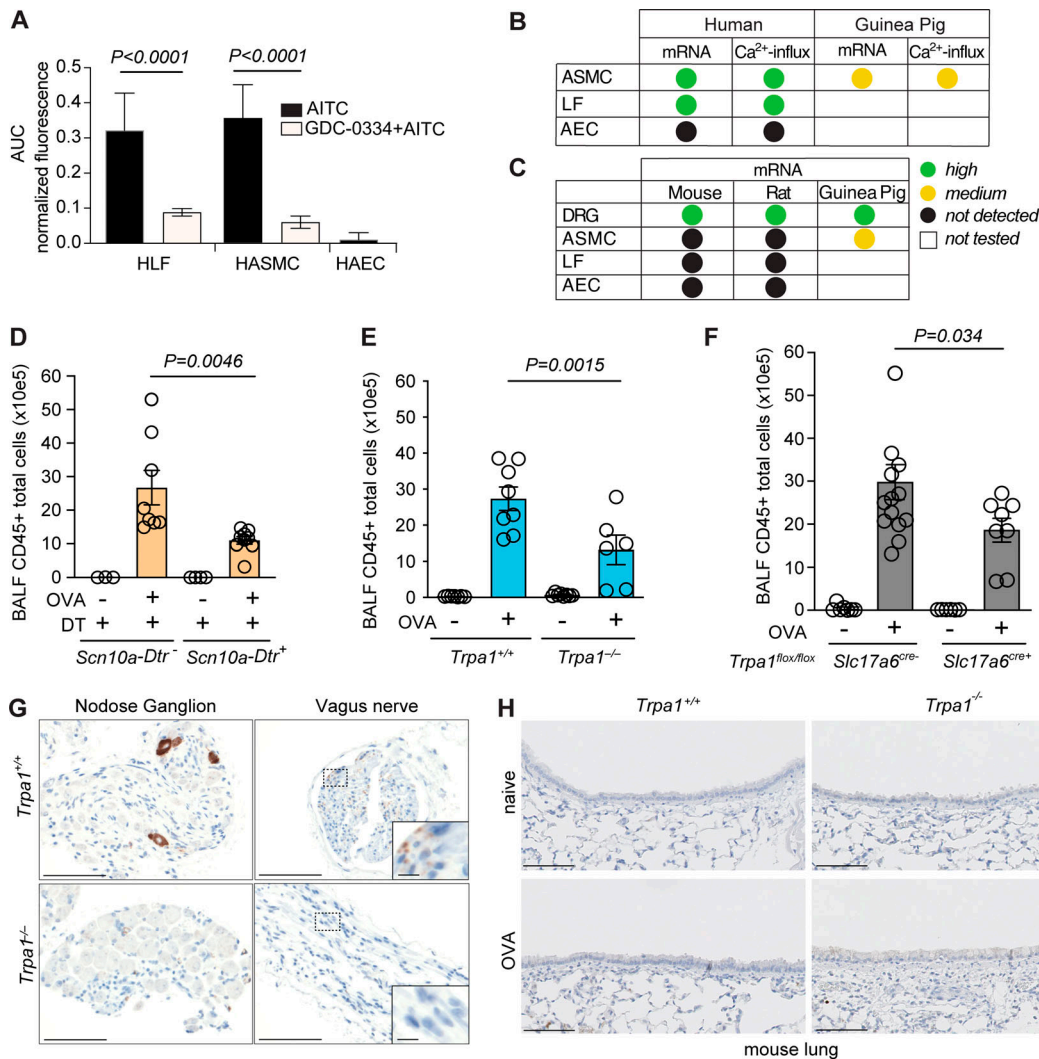


Figure 1. Expression pattern and functionality of neuronal and nonneuronal TRPA1 in the lungs across species. (A) Calcium influx responses to AITC in the presence or absence of GDC-0334, from HASMCs, HLFs, and HAECs. Graphs represent normalized AUC (two-tailed unpaired *t* test). Five biological replicates were performed. A total of 75–120 cells/biological replicates were analyzed. Data are expressed as the mean \pm SD. **(B and C)** Summary of TRPA1 expression and calcium influx in primary cells from human and preclinical species. **(D–F)** Analysis of leukocyte infiltration in the BALF of OVA-challenged or unchallenged mice from *Scn10a-Dtr⁻* (D), *Trpa1^{+/+}* or *Trpa1^{-/-}* (E), and *Trpa1^{lox/lox} Slc17a6^{cre+}* or *Trpa1^{lox/lox} Slc17a6^{cre-}* (F) mice. Data are expressed as the mean \pm SEM; *n* \geq 8 animals per group. A comparison for each pair was performed using one-way ANOVA or two-tailed *t* test. **(G and H)** TRPA1 immunostaining of *Trpa1^{+/+}* or *Trpa1^{-/-}* mice. Scale bars = 100 μ m. **(G)** Nodose ganglia and vagus nerve. The insets depict a higher magnification of the axons of nodose neurons. Scale bar = 10 μ m. **(H)** Lung sections of naive and OVA-challenged mice. AEC, airway epithelial cell; ASMC, Airway smooth muscle cell; LF, lung fibroblast.

The vast majority of the nociceptors innervating the airways are of vagal origin, with somas located in the nodose ganglia (Nassenstein et al., 2008). Vagal nociceptors express the vesicular glutamate transporter 2 (Vglut2, encoded by the gene *Slc17a6*; Chang et al., 2015). Thus, we generated *Slc17a6-cre⁺ Tdt⁺* (*Slc17a6-Tdt*) mice, in which nodose sensory neurons display bright tdTomato fluorescence. Whole-mount three-dimensional lung imaging confirmed that the vast majority of lung innervation was coming from nodose neurons (Fig. S2 D and data not shown). *Slc17a6-cre⁺* were then crossed to *Trpa1^{lox/lox}* mice to delete TRPA1 selectively in the nodose sensory neurons of their offspring (*Slc17a6-cre⁺ Trpa1^{lox/lox}* mice; Fig. S2 E). The reduction of OVA-induced eosinophil-rich BALF infiltrates was similar in global and nodose neurons-specific *Trpa1* genetic deletion (Fig. 1,

E and F; and Fig. S2 F). In line with these results, TRPA1 expression was confirmed in mTRPA1-transfected Chinese hamster ovary (CHO) cells and nodose ganglia neurons' somas and axons (vagus nerve) but was not detected in lungs from *Trpa1^{+/+}* mice after OVA challenge (Fig. 1, G and H; and Fig. S2, G and H), demonstrating the predominant role of nodose nociceptors in regulating TRPA1-dependent airway inflammation in mice.

GDC-0334 is suitable for evaluation as an orally bioavailable TRPA1 inhibitor across multiple species

The preclinical results in mice revealed the potential of targeting TRPA1 for the treatment of asthma and initiated development of a SMI for oral therapy. The search focused on identification of a SMI that blocks TRPA1 function in humans and across several

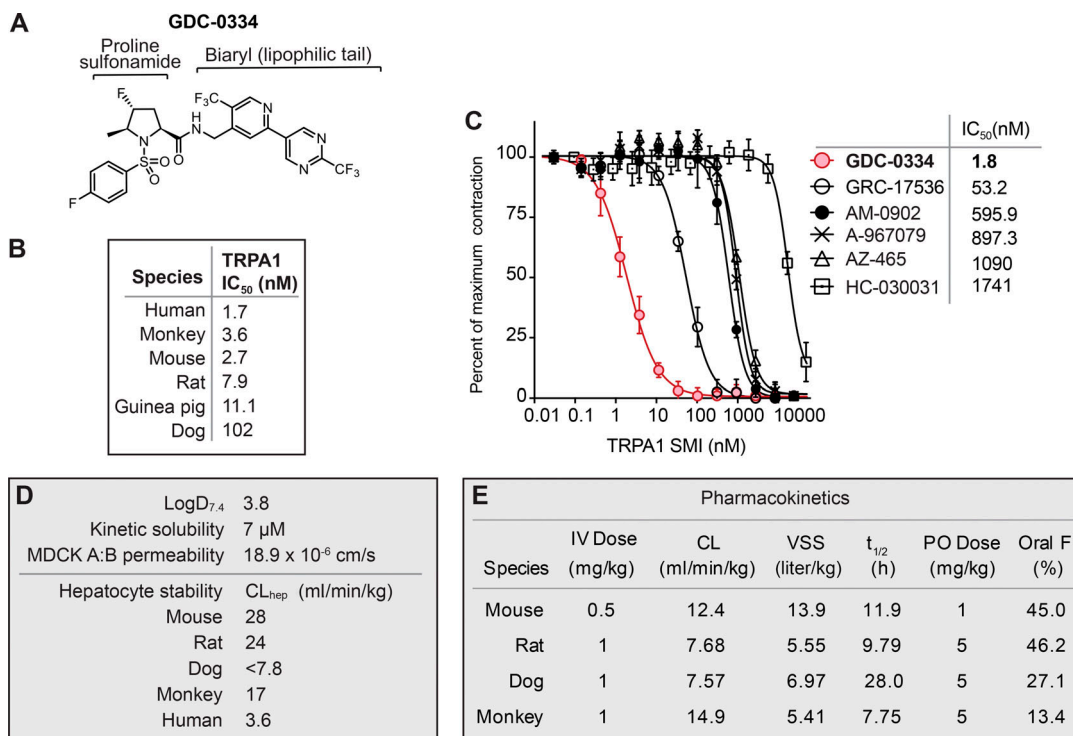


Figure 2. **In vitro and in vivo binding properties of GDC-0334 are consistent with a potent, specific, and orally bioavailable TRPA1 inhibitor.** (A) Structure of GDC-0334. (B) Cross-species TRPA1 potencies of GDC-0334 as measured in CHO cell line-based fluorometric imaging plate reader Ca²⁺ assays. (C) Inhibitory dose–response curves of TRPA1 antagonists (Table S1 B) on HASMC contraction assay. (D) Physicochemical and in vitro ADME properties of GDC-0334. (E) Cross-species IV/oral (PO) PK parameters of GDC-0334. CL, clearance; CL_{hep}, hepatic clearance of drug; IV, intravenous; VSS, volume of distribution; F, bioavailability.

preclinical species that together could recapitulate multiple mechanisms of action of TRPA1 in asthma. GDC-0334, a member of the proline sulfonamide class of TRPA1 antagonists, was identified through a medicinal chemistry campaign (Chen et al., 2018; Fig. 2 A). Consistent with other reported TRPA1 inhibitors (Skerratt, 2017), proline sulfonamide-based inhibitors are characterized by poor aqueous solubility and oral bioavailability (Chen et al., 2018). Despite efforts to improve solubility by lowering lipophilicity (i.e., logD_{7.4}), identification of compounds with sufficient TRPA1 potency was not possible in this physicochemical space. Instead, increasing lipophilicity relative to previous generation inhibitors by adding a highly fluorinated biaryl group (Fig. 2 A) led to improved potency measured in a TRPA1 agonist (cinnamaldehyde [CA])–based calcium flux assay. GDC-0334 demonstrated potent TRPA1 inhibition in several species, including human (half-maximal inhibitory concentration [IC₅₀]: 1.7 nM), cynomolgus (cyno) monkey (3.6 nM), mouse (2.7 nM), guinea pig (11.1 nM), and dog (102 nM; Fig. 2 B), with good selectivity against human TRPV1, TRPM8, and TRPC6 (all IC₅₀s >10 μM; Fig. 2 B and Table S1 A). Furthermore, GDC-0334 inhibited calcium flux in human primary cells, HASMCs and HLFs, treated with the TRPA1 agonist AITC (Fig. 1 A and Fig. S1, B and D).

As ASM hypertrophy and contraction are key contributors to asthmatic airway constriction, the effects of GDC-0334 were further explored in an impedance-based cell assay using HASMCs whereby exposure to a TRPA1 agonist induces

cellular contraction quantified by changes in cellular impedance (Bravo et al., 2018; Fig. 2 C). GDC-0334 blocked HASMC contraction with an IC₅₀ of 1.8 nM, which was significantly more potent than that of other TRPA1 inhibitors reported in the literature (Nyman et al., 2013; Schenkel et al., 2016; Skerratt, 2017; Fig. 2 C and Table S1 B).

GDC-0334 possessed favorable in vitro properties, including high passive permeability in Madin Darby canine kidney (MDCK) cells (P_{app} A-to-B = 18.9 × 10⁻⁶ cm/s) and moderate to high metabolite stability in cross-species hepatocytes (Fig. 2 D). When tested in vivo, GDC-0334 displayed low to moderate clearances with relatively large volumes of distribution (5.41–13.9 liter/kg) for a neutral molecule, ultimately translating to long in vivo half-lives (7.75–28 h) across preclinical species (Fig. 2 E). Most notably, GDC-0334 possessed acceptable oral bioavailability (13–46%) following oral dosing in preclinical species (Fig. 2 E) despite low kinetic solubility (7 μM) in aqueous buffer (Fig. 2 D). Taken together, the absorption, distribution, metabolism, and excretion (ADME) properties of GDC-0334 were consistent with an orally bioavailable drug suitable for both the preclinical evaluation of small molecule inhibition of TRPA1 in asthma models and ultimately translation to clinical trials in humans.

Structure of GDC-0334–bound TRPA1 reveals transmembrane binding site

To better understand the mechanism of action of GDC-0334, its binding mode was evaluated via cryogenic electron microscopy

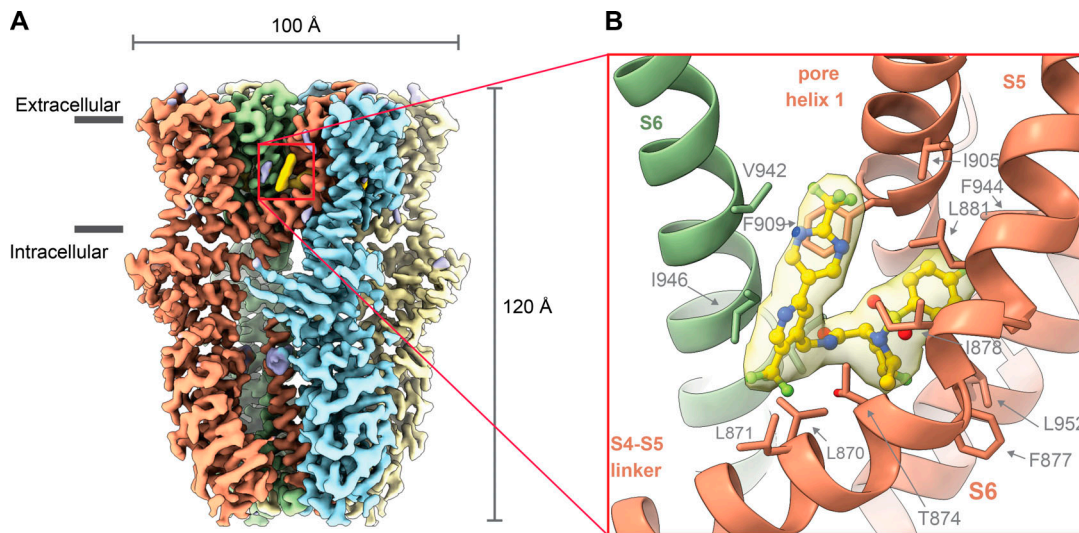


Figure 3. CryoEM reveals binding of GDC-0334 to the human TRPA1 transmembrane domain. (A) The cryoEM map of human TRPA1 in complex with GDC-0334 in an isosurface rendering. TRPA1 protomers are colored red, green, pale yellow, and blue; GDC-0334 is in bright yellow. Map features without assigned atomic structures are colored purple. Gray bars indicate the approximate locations of the membrane boundaries. **(B)** Side chains involved in contacts with GDC-0334 are shown in stick representation. The cryoEM map surrounding the ligand is shown in a transparent isosurface representation.

(cryoEM). A three-dimensional map of GDC-0334 bound to human TRPA1 (Fig. 3, A and B; and Fig. S3) at a resolution of 3.6 Å revealed a deep binding pocket entirely buried in the transmembrane domain of TRPA1, approximately midway across the membrane bilayer. Within this binding pocket, the proline sulfonamide portion of GDC-0334 is encased by multiple elements of one TRPA1 subunit (S5 helix, S6 helix, pore helix 1, and the S4-S5 linker) and positioned similarly to the smaller antagonist A-967079, above the S5 elbow (Paulsen et al., 2015). The fluorinated biaryl group of GDC-0334 protrudes outward and aligns along the S6 helix of the neighboring TRPA1 subunit with one side, but its other side appears largely exposed to the membrane environment and does not interact directly with TRPA1. In total, ~20 amino acid side chains, most of them apolar, are involved in forming the inhibitor binding pocket. Extensive van der Waals contacts are made through residues of the S4-S5 linker. Notably, each S6 transmembrane helix is contacted by two ligand molecules through two distinct sets of interactions with side chains on either side of the S6 helix. The conformation of TRPA1 seen in this structure suggests that GDC-0334 binds to a closed state of TRPA1 and acts as a molecular wedge to restrict the conformational changes associated with gating, including straightening of the S5 elbow and twisting and upward shift of S6 (Zhao et al., 2020). Taken together, the location and binding mode of GDC-0334 suggests a membrane-access mechanism whereby the SMI must first partition into the phospholipid membrane bilayer before reaching and interacting with the inhibitor binding site. This mechanism of action is consistent with the required lipophilicity, high volumes of distribution, and characteristic poor aqueous solubility of the proline sulfonamide class of GDC-0334 (Fig. 3 A), wherein the fluorinated biaryl likely serves as a lipophilic tail necessary for partitioning into the lipid membrane.

GDC-0334 treatment reduces AITC-induced vascular leakage in rats

Vascular edema is a well-established component of neurogenic inflammation that contributes to the underlying pathophysiology in asthma (Chiu et al., 2012). Application of TRPA1 agonists to the skin activates TRPA1 channels at the terminals of the sensory neurons, leading to the local release of neuropeptides that act on local vascular cells to induce vasodilation, vascular leakage, and edema and activate local immune cells to amplify neurogenic inflammation (Aubdool et al., 2016). The contribution of TRPA1 to vascular leakage was evaluated by near-infrared fluorescent imaging (NIRF), in which perfusion of an injected fluorescent dye was imaged after topical application of AITC to the ear of *Trpa1*^{+/+} or *Trpa1*^{-/-} rats (Fig. 4 A). Topical application of 5% AITC significantly increased NIRF dye perfusion in *Trpa1*^{+/+} rats, but this effect was diminished in *Trpa1*^{-/-} rats (Fig. 4 B). Next, GDC-0334 was dosed at 1, 3, and 10 mg/kg in rats 3 h before topical application of AITC. Dose-dependent reductions in Evans blue perfusion were observed (Fig. 4, C and D), demonstrating that GDC-0334 blocks TRPA1-mediated vascular leakage.

GDC-0334 treatment reduces airway inflammation in rats and guinea pigs as well as cough in guinea pigs

The effect of GDC-0334 on OVA-induced airway inflammation was next evaluated (Fig. S4 A). Rats received a daily oral dose of GDC-0334 3 h before each OVA challenge for peak plasma drug concentrations at the time of challenge (Fig. S4 B). Total cells, eosinophils, and neutrophils in BALF were increased 24 h after the last OVA challenge in the vehicle-treated rats, whereas GDC-0334 reduced BALF infiltrates numbers in a dose-dependent manner (Fig. 5 A and Fig. S4 E). GDC-0334 treatment significantly blunted an increase of the neuropeptide substance P (SP) in the BALF after OVA challenge (Fig. S4 F), indicating that

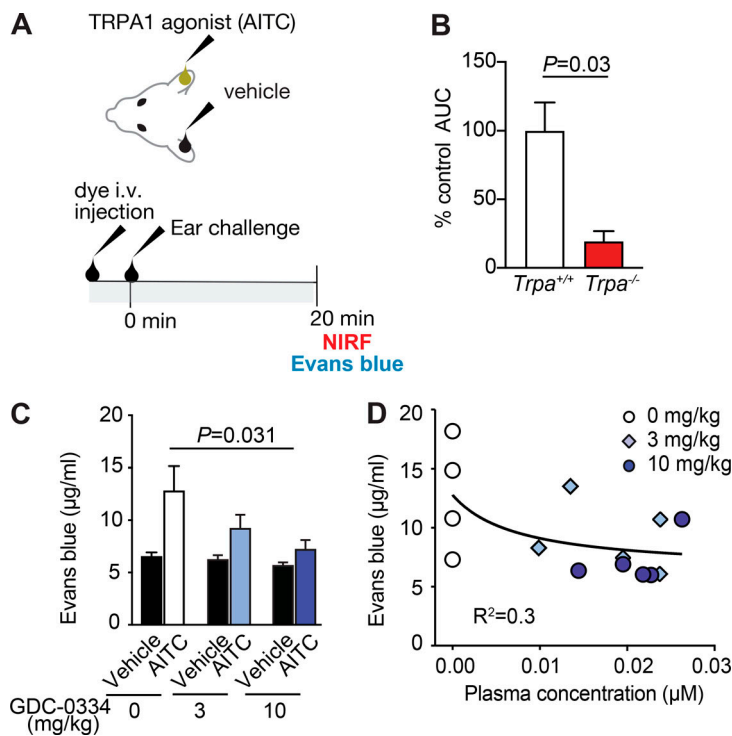


Figure 4. GDC-0334 suppresses AITC-induced edema in vivo rat. (A) Experimental outline of vascular permeability (measured by NIRF [B] or Evans blue [C]) after AITC or vehicle application. (B and C) Normalized AUC from 5–20 min after AITC application. (B and C) Data are expressed as the mean \pm SD; $n = 4$ –6 animals per group; two-tailed unpaired t test. (D) GDC-0334 plasma concentration and vascular permeability correlation. $n = 4$ or 5/group. Curve fitting was obtained by a four-parameter nonlinear regression. Dex, dexamethasone.

allergen-induced neurogenic inflammation in the lung can be inhibited by GDC-0334.

The lung physiology of guinea pigs resembles that of humans, including neutrophilic and eosinophilic airway disease, bronchospasm, and neuronal reflexes (Canning et al., 2014; Canning and Chou, 2008). In the OVA airway challenge model, a single oral administration of 70 mg/kg GDC-0334 significantly reduced BALF infiltrates to the airways (Fig. 5 B and Fig. S4 G). The effect of GDC-0334 on activation of vagal nerves in the guinea pig airway was next evaluated using the CA-induced cough model (Fig. S4 H). Guinea pigs were dosed with GDC-0334 (5, 15, or 45 mg/kg) or vehicle control before airway challenge with CA, and coughs were counted for the subsequent 30 min. The CA-evoked number of coughs over 30 min was significantly reduced in a dose-dependent manner in guinea pigs treated with GDC-0334 compared with vehicle (Fig. 5, C and D; and Fig. S4 I). Latency to the first cough also tended to be longer in guinea pigs treated with GDC-0334 compared with the vehicle group (Fig. S4 J). Collectively, these findings underscore the effect of TRPA1 inhibition on allergen-induced airway inflammation and cough.

Pharmacodynamic (PD) modulation of AITC-induced dermal blood flow (DBF) by GDC-0334 in guinea pigs and rats

Blood perfusion is a component of vascular edema that can be measured in clinical settings using laser speckle contrast imaging (LSCI). We previously showed that the DBF response to AITC is similarly observed in rodents and humans (Joseph et al., 2020). Topical application of AITC to the ear of *Trpa1*^{+/+}, but not *Trpa1*^{-/-} rats, increased DBF above baseline, confirming that AITC-induced DBF is TRPA1 dependent (Fig. 6, A and B; and Fig. S5 A).

Next, GDC-0334 was dosed in rats or guinea pigs at 3 and 3.5 h before AITC skin challenge, respectively. Untreated rats

had robust increases in DBF, which was reduced in rats dosed with GDC-0334 before AITC application (Fig. 6 C). Dose-dependent decreases in the DBF rise-times and maximal levels were observed (Fig. 6, D and E; and Fig. S5 B). Likewise, in guinea pigs GDC-0334 treatment caused a dose-dependent reduction in AITC-induced DBF (Fig. 6, F–H). Taken together, these data supported the use of AITC-induced DBF as a PD biomarker for GDC-0334 in human clinical trials.

GDC-0334 dose proportionally inhibits AITC-induced DBF, pain, and itch in healthy human subjects

Guided by the in vitro and in vivo pharmacokinetics (PK)/PD properties of GDC-0334 in preclinical species, the PK profile and PD effects of GDC-0334 were explored in a Phase 1 study of healthy volunteers. We previously described the development of an AITC skin challenge model in humans as a PD biomarker of TRPA1 activity. In this model, 10% and 15% AITC applied to the forearm induces transient local pain, itch, and DBF that can be quantified with LSCI (Fig. 7 A; Joseph et al., 2020).

In a randomized, double-blind, single-ascending dose (SAD) study in healthy volunteers, placebo control or GDC-0334 was dosed orally, and AITC skin challenge was performed 3–8 h after dosing (Fig. 7 A). Each cohort consisted of six subjects dosed with GDC-0334 and two subjects dosed with placebo. GDC-0334 was well tolerated with only mild or moderate adverse events (AEs), and no serious treatment-emergent AEs (TEAEs), AEs of special interest, TEAEs leading to death, or TEAEs leading to study withdrawal were reported in any of the subjects. No TEAEs were thought to be related to GDC-0334 treatment with the exception of one case of mild headache. Based on these results, we cannot anticipate any potential risks consequent to prolonged exposure to TRPA1 inhibitor; however, this requires evaluation in a larger

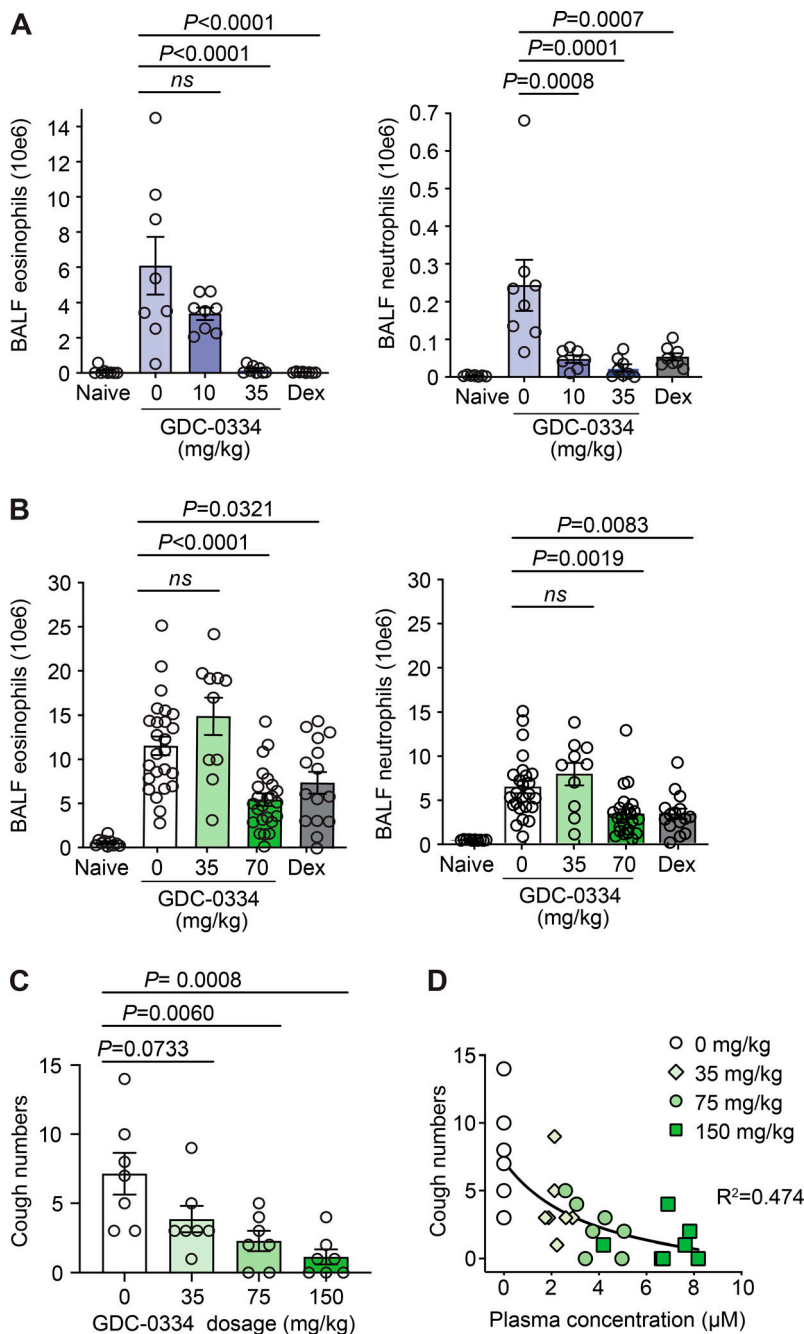


Figure 5. GDC-0334 is efficacious in rat and guinea pig in vivo models of airway allergic inflammation and cough. (A and B) Total eosinophil and neutrophil cell counts from BALF of naive or OVA-challenged rats (A) or guinea pigs (B) pretreated with GDC-0334. Data are expressed as the mean \pm SEM; $n = 5$ –30 animals per group. Comparison for each pair was performed using one-way ANOVA. **(C)** CA-evoked cough in guinea pigs pretreated with GDC-0334. Data are expressed as the mean \pm SEM; $n = 7$ /group. Comparison for each pair was performed using one-way ANOVA. **(D)** Graph representing the correlation of the GDC-0334 dosage and its antitussive effects in guinea pigs. $n = 6$ /group. Curve fitting was obtained by a three-parameter nonlinear regression.

cohort of patients. GDC-0334 was absorbed at variable times to reach max concentration (T_{\max}), with max concentration (C_{\max}) occurring at median 3.5 to 7.0 h (range, from 1.5 to 24 h). Approximately dose-proportional increases in GDC-0334 exposures, measured as C_{\max} , area under the curve (AUC)_{0–24h}, and AUC _{0–72h}, were observed when dose increased from 75 mg to 600 mg (data not shown). Similar to preclinical species, GDC-0334 had a strong PD effect on the DBF response to the AITC skin challenge in human subjects (Fig. 7, B–D; and Fig. S5 C). Near-complete inhibition of AITC-induced DBF was observed in subjects with GDC-0334 plasma concentrations greater than ~ 250 ng/ml (Fig. 7 D), or 4.92 nM free plasma concentrations, which is sufficient to achieve >50% inhibition of the TRPA1-agonist HASMC contraction assay

($IC_{50} = 1.8$ nM) or CA-based calcium flux hTRPA1 assay ($IC_{50} = 1.7$ nM). Thus, the drug exposures that effectively inhibited AITC-induced DBF as observed after the 600-mg dose in humans may also lead to a reduction in lung smooth constriction in patients with asthma.

TRPA1 mediates pain and itch in response to AITC in pre-clinical models, but as of yet, this has not been confirmed in humans. In a rat preclinical study, GDC-0334 reduced AITC-induced nocifensive behavior in a dose-dependent manner (Fig. S5 D), with suppression comparable to that of *Trpa1*^{-/-} rats at the 3-mg/kg dose of GDC-0334 (Reese et al., 2020). Human subjects in the Phase 1 study were asked to verbally rate pain and itch on a scale of 0–10 after application of AITC to the forearm

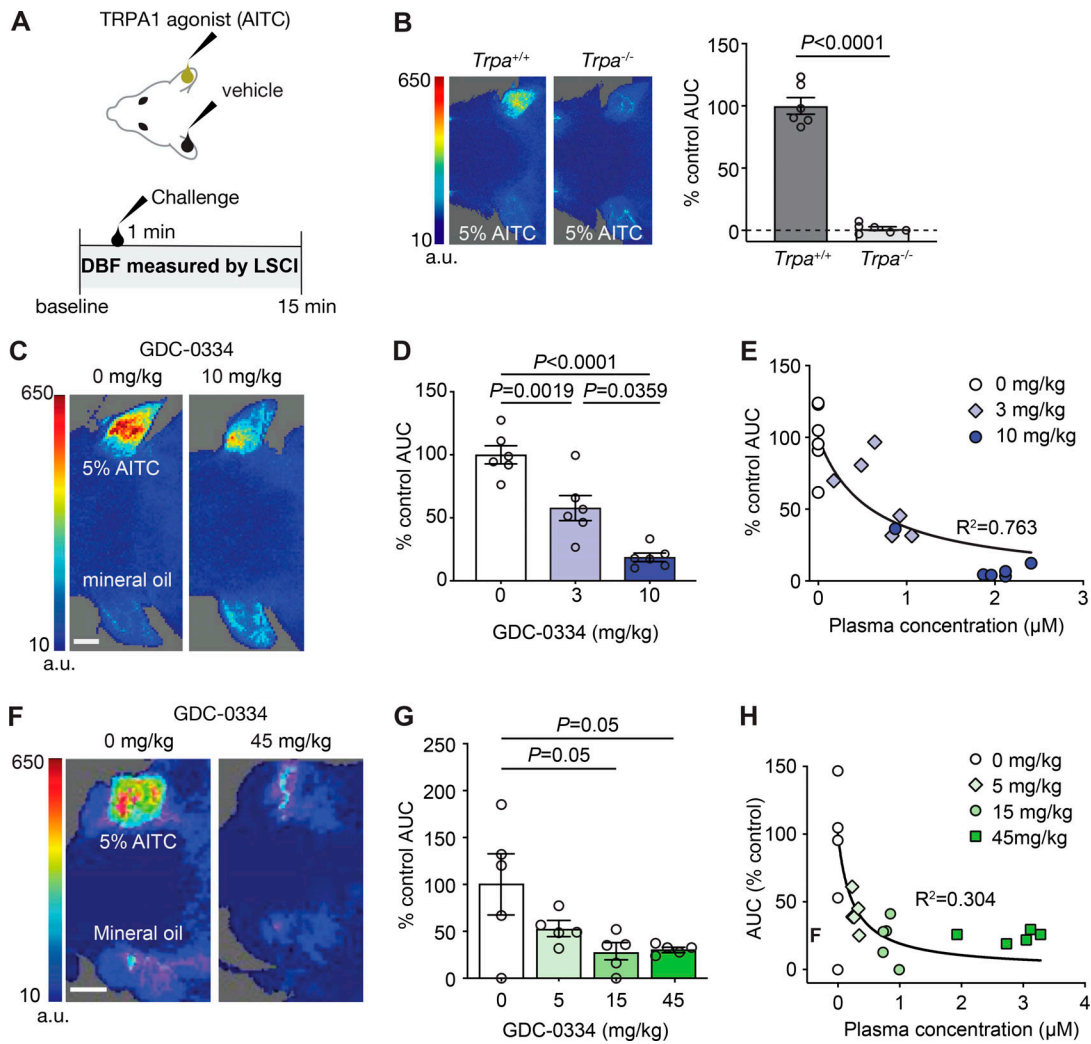


Figure 6. **GDC-0334 is a potent inhibitor of AITC-induced DBF in vivo in rats and guinea pigs.** (A) Experimental outline of LSCI for B–H. (B) Representative flux signal 5 min after AITC or vehicle application in *Trpa*^{+/+} and *Trpa*^{-/-} rats; normalized DBF AUC from 1–5 min after AITC application. The dashed line indicates 0%. Data are expressed as the mean ± SEM; *n* = 6 animals per group; two-tailed unpaired *t* test. (C) Representative flux signal 5 min after AITC application in a rat dosed with vehicle GDC-0334. Scale bar = 5 mm. (D) Dose-dependent reduction in normalized AUC in rats pretreated with GDC-0334 following AITC challenge (one-way ANOVA; *P* < 0.0001; *F* = 30.9; Tukey post hoc tests). Data expressed as the mean ± SEM; *n* = 6 animals per group. (E) GDC-0334 plasma and DBF correlation. Mean ± SEM; *n* = 6/group. Curve fitting was obtained by a three-parameter nonlinear regression. (F) Representative flux signals AITC application in guinea pigs treated with vehicle or 45 mg/kg GDC-0334. Scale bar = 10 mm. (G) GDC-0334 dose dependently reduced normalized AUC from 1 to 5 min after AITC application (one-way ANOVA; *P* = 0.026; *F* = 4.032; Tukey post hoc tests). Data expressed as the mean ± SEM; *n* = 4 or 5 animals per group. (H) Correlation of GDC-0334 plasma concentrations and AUC levels. *n* = 5/group. Curve fitting was obtained by a three-parameter nonlinear regression. a.u., arbitrary unit.

(Fig. 7 A). Similar to DBF, GDC-0334 dose dependently reduced AITC-induced pain and itch compared with placebo-treated subjects, with near-complete inhibition observed in subjects dosed with 600 mg GDC-0334 (Fig. 7, E and F; and Fig. S5, E and F). In summary, these results provide clinical evidence that treatment with an oral TRPA1 inhibitor reduces DBF and self-reported pain and itch induced by a TRPA1 agonist in human subjects.

Discussion

The tissue pathophysiology associated with asthma is very complex. An increasing number of preclinical and human studies

show that regulation of neural activation in the airways could be an effective therapeutic strategy (Belvisi et al., 2016; Drake et al., 2018; Mazzone and Undem, 2016). In particular, nociceptors, through the local release of neuropeptides such as the tachykinins SP and neurokinin A (NKA), and calcitonin gene-related peptide (CGRP) contribute to many of the traits associated with asthma. Tachykinin levels are increased in asthmatics and are potent inducers of bronchoconstriction, airway secretions, and neurogenic inflammation through their activity on neurokinin (NK) receptors (Cardell et al., 1994; Chiu et al., 2012; Chu et al., 2000; Fischer et al., 1996; Kay et al., 2007; Mostafa et al., 2008; Tomaki et al., 1995). Several studies show increased expression of NK receptors in lungs from humans with asthma, and

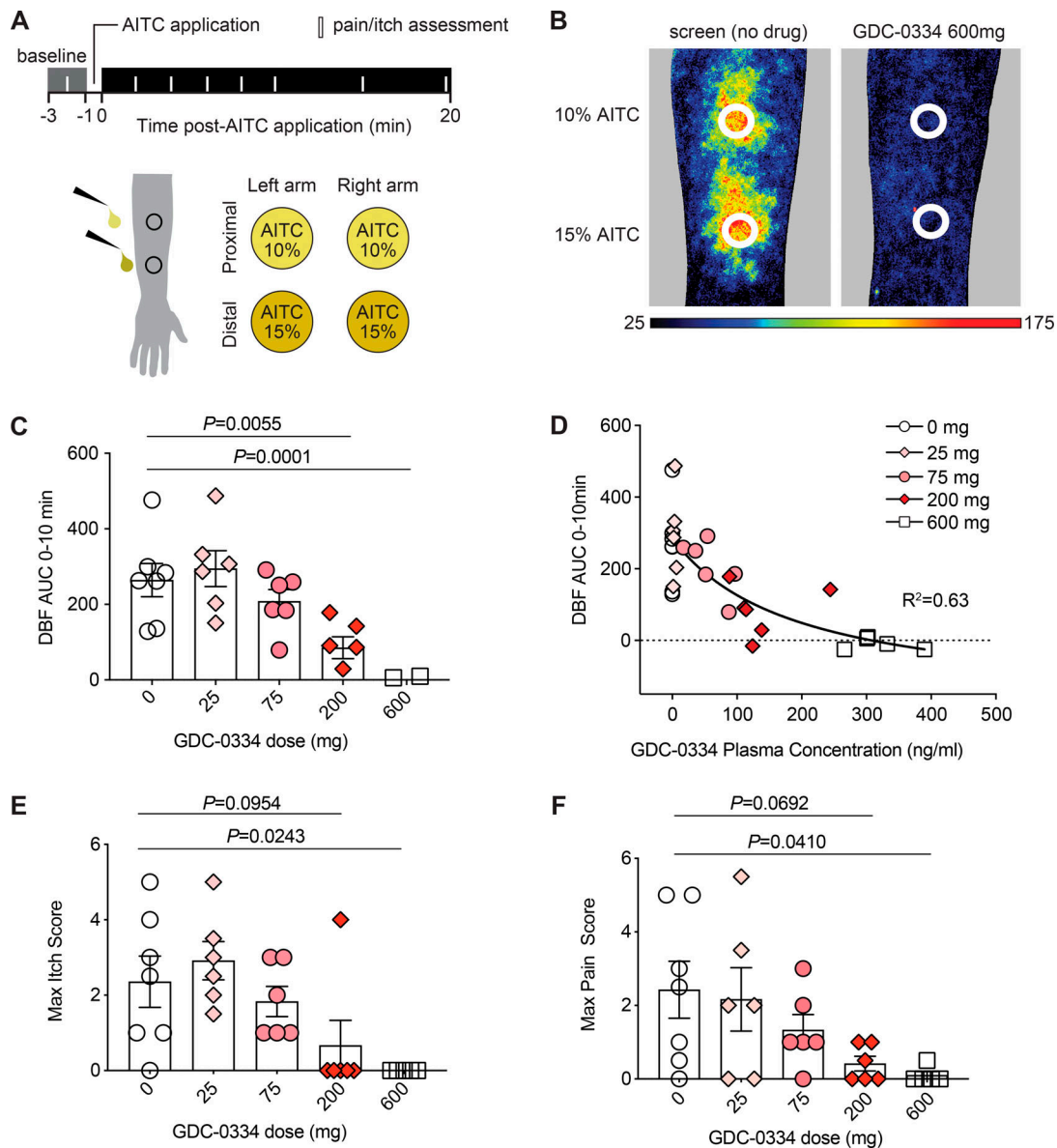


Figure 7. **GDC-0334 target engagement in humans.** (A) Schematic of experimental design. (B) Representative flux signals from the same person when an AITC skin challenge was conducted on screen day (no drug) or after dosing with GDC-0334. Images were taken 5 min after AITC application. (C) Comparison of AITC-induced DBF AUC from 0 to 10 min in subjects dosed with placebo or GDC-0334. Data shown as mean ± SEM; n = 7 (0 mg), 6 (25 mg), 6 (75 mg), 6 (200 mg), or 5 (600 mg). Dunnett's multiple comparison test used for statistical analysis to compare each GDC-0334 dose group with 0 mg. (D) Plasma concentrations relative to DBF AUC 0-10 min. n = 5 or 6/group. R^2 determined by [inhibitor] versus response (three parameters) nonlinear regression. The dashed line indicates an AUC of 0. (E) Comparison of max itch induced by AITC in subjects dosed with placebo or GDC-0334. Data shown as mean ± SEM; n = 7 (0 mg), 6 (25 mg), 6 (75 mg), 6 (200 mg), or 5 (600 mg); Dunnett's multiple comparison test. (F) Comparison of maximum pain induced by AITC in subjects dosed with placebo (0 mg) or GDC-0334. Data shown as mean ± SEM; n = 7 (0 mg), 6 (25 mg), 6 (75 mg), 6 (200 mg), or 5 (600 mg); Dunnett's multiple comparison test.

inhalation of NKA induces airway bronchoconstriction (Bai et al., 1995; Chu et al., 2000; Joos et al., 1987). In clinical studies, several antagonists of NK receptors reduced NKA-induced AHR, but none had an effect on AHR, cough, or airway inflammation induced by nonspecific stimuli (Fahy et al., 1995; Joos et al., 2004; Schelfhout et al., 2006; Van Schoor et al., 1998). The disappointing efficacy could be related to poor PK and low potency, overlapping and redundant tachykinin signaling through NK receptors and the recently discovered SP receptor Mrgprx2, or other neuropeptides that were not blocked with these approaches

(Green et al., 2019; Kay et al., 2007). Thus, the failure of NK receptor antagonists in the clinic does not rule out the potential role of vagal nociceptors in asthma and shifts attention toward looking for other ways to modulate their activation.

A promising approach to target vagal nociceptor activity is through inhibition of TRP channels. TRP channel activation induces cough and neurogenic inflammation. Asthmatics have heightened cough reflex sensitivity to inhaled capsaicin, a TRPV1 ligand (Satia et al., 2017; Satia et al., 2019), suggesting that vagal nociceptors exist in a hypersensitive state in asthmatic

airways. Of the TRP channels, TRPA1 has the broadest array of known stimuli, including many environmental stimuli known to aggravate asthma symptoms and endogenous inflammatory mediators found in the airways of asthmatics.

The results shown here revealed that selective deletion of the *Trpa1* gene in nodose neurons suppresses immune response similarly to constitutive *Trpa1*^{-/-} mice (Fig. 1, E and F; and Fig. S2, C and F). Furthermore, we could not reproduce previously published observations (Nassini et al., 2012) of TRPA1 expression in nonneuronal cells in mouse lungs, formally demonstrating that TRPA1 activation in vagal nociceptors, and no other lung resident cells, contributes to airway inflammation in mice (Fig. 1, F-H; and Fig. S2, C and F-H). The discrepancy between Nassini et al. (2012) and our results could be because the antibody used by Nassini et al. may lack specificity for mouse TRPA1. Of note, a recent report suggests that the specificity of some of the most-cited anti-TRPA1 antibodies should be revisited (Virk et al., 2019). However, the presence of functional TRPA1 channels in HASMCs and HLFs was confirmed (Fig. 1, A and B; Virk et al., 2019). Thus, in asthmatic airways, endogenous or exogenous agonists could activate TRPA1 expressed by HASMCs, HLFs, and vagal nociceptors.

Many pharmaceutical companies have reported discovery of TRPA1 chemical matter; however, identifying high-quality orally available molecules with good ADME properties suitable for clinical progression has been challenging (Skerratt, 2017). During the course of our discovery efforts, common strategies to improve solubility, such as reducing lipophilicity, often resulted in a concomitant loss of TRPA1 potency, suggesting that lipophilic character is an essential property of the proline sulfonamide class of inhibitors. In agreement with this hypothesis, the highly fluorinated lipophilic biaryl of GDC-0334 (Fig. 2 D) provides high potency across assays (Fig. 2, B and C). In addition to excellent potency, GDC-0334 also possesses highly optimized ADME properties and acceptable oral bioavailabilities across species (Fig. 2, D and E), making it suitable not only for investigation in preclinical species but also as a potential human therapeutic. A cryoEM structure of GDC-0334 bound to TRPA1 enabled structure-based drug design and elucidated the mechanism of action of proline sulfonamide-based inhibitors of TRPA1. Based on this unique binding mode, it is likely that GDC-0334 must first partition into the lipid bilayer before interacting with the TRPA1 binding site and that the observed potency of GDC-0334 is driven by both interactions with TRPA1 and its ability to partition into the membrane. While this membrane-access mechanism was previously described for a number of drugs targeting membrane receptors (Vauquelin and Packeu, 2009), other recent cryoEM structures of ion channels bound with small molecule modulators at the protein-lipid interface (Gao et al., 2016; Liu et al., 2019) suggests that this mechanism may play a larger role in small molecule drug action than commonly appreciated.

A significant challenge for the development of therapeutics for asthma is the lack of preclinical models that reflect human asthma. Thus, a combinatorial approach was used to evaluate the effect of GDC-0334 on asthma traits in several relevant *in vitro* and *in vivo* models. ASM contraction has long been

recognized as contributing to the bronchoconstriction and AHR characteristic of asthma. Thus, potency of GDC-0334 was evaluated in cultured HASMCs where it stood out as one the most potent TRPA1 inhibitors tested (Fig. 2 C). This observation in combination with favorable ADME properties (Fig. 2, D and E) suggests that oral administration of GDC-0334 could alleviate bronchoconstriction directly by inhibiting TRPA1 activity in smooth muscle of the lower airways.

Tachykinins and CGRP released by nociceptors upon TRPA1 activation can also initiate neurogenic inflammation featuring vasodilatation, vascular leakage, edema, and an increase of inflammatory infiltrates (Chiu et al., 2012). GDC-0334 blocked vascular leakage in rats, suggesting that its administration would reduce edema in asthmatics (Fig. 4, C and D). Neutrophilia in the airways is associated with disease severity and airflow limitation in humans, but it is not recapitulated in OVA-induced inflammation models in mice. Neutrophil infiltration is robust in guinea pigs, where GDC-0334 oral administration led to the reduction of both eosinophil and neutrophil numbers in the BALF (Fig. 5, A and B), indicating that GDC-0334 could be a therapeutic approach for asthmatics whose disease features increased eosinophils and/or neutrophils in the airways.

Cough is a defining symptom of asthma, and cough variant asthma is an established asthma phenotype for which there are few effective therapeutics (Smith, 2010). Cough symptoms may indicate that underlying neuronal hypersensitivity is a key driver of disease in these patients. Since activation of TRPA1 directly induces cough, TRPA1 inhibition could have great efficacy in patients with cough variant asthma (Belvisi and Birrell, 2017). Aerosolized CA challenge in guinea pigs is a model widely used to study the cough response mediated by TRPA1 *in vivo*. In this model, oral administration of GDC-0334 reduced both number of coughs and latency to the first cough induced by CA in a dose-dependent manner (Fig. 5, C and D; and Fig. S4, I and J). This fast response is most likely due to the activation of the TRPA1 channels expressed by vagal nociceptors with terminals strategically located close to the airway epithelium, ready to detect any potential exogenous noxious stimulus. Cough challenge studies with suitable challenge agents would be an ideal design to evaluate pharmacologic activity of GDC-0334 in the airways but may not necessarily predict efficacy on natural cough symptoms in patients (Khalid et al., 2014).

Translation of preclinical findings to clinical efficacy is a key hurdle for drug development. Taking advantage of the TRPA1 channels expressed by skin-innervating DRG nociceptors, we developed an AITC-induced DBF skin challenge model that is a translational and noninvasive method to quantify TRPA1 PD effects on edema in rodents and humans (Fig. 6 and Fig. 7). Results from the GDC-0334 Phase 1 study confirm that AITC-induced DBF is mediated by TRPA1 in humans (Fig. 7 and Fig. S5 C). In both humans and rodents, the GDC-0334 PK/PD relationship followed a similar pattern (Fig. 6 and Fig. 7), indicating that AITC-induced DBF is a target engagement biomarker suitable for future screening of TRPA1 inhibitors in preclinical species with high predictive value for PD activity in humans.

More studies are necessary to understand the relationship between the skin and the lung for asthma. The difference in dose

response for TRPA1-mediated neurogenic inflammation in the skin versus TRPA1-mediated lung inflammation or cough may indicate different target cells (sensory neurons and/or smooth muscle cells) or location of inhibition (sensory nerve endings or nerve bodies). Thus, the AITC-induced DBF model provides evidence of peripheral TRPA1 target engagement by GDC-0334 but may not necessarily predict exposures needed for efficacy in asthma or other indications. The plasma concentrations required for near-complete inhibition of AITC-induced DBF in humans as observed after dosing with 600-mg GDC-0334 exceeded the IC_{50} for HASMC contraction dependent on TRPA1, suggesting that reduction of lung smooth muscle contraction is possible in humans with asthma.

Translatability of preclinical models of pain and itch to humans is uncertain (Burma et al., 2017). Similar to rats with TRPA1 genetic deficiency, GDC-0334 reduced rat paw flinching induced by AITC application (Fig. S5 D). Likewise, in humans, pain and itch were reduced by GDC-0334 treatment in a dose-proportional manner (Fig. 6). Recently, the commercially available TRPA1 inhibitor A-967079, which is ~500 times less potent than GDC-0334 (Fig. 2 C), was shown to reduce localized pain induced by the synthetic TRPA1 agonist JT010 when administered together by intradermal injection (Heber et al., 2019). Translatability of this model between preclinical species and humans is unclear. Further, the DBF response to intradermally injected JT010 should be assessed, as DBF is a more objective and quantitative biomarker than self-reported pain for use in PK/PD modeling to inform dose selection. Future studies are needed to evaluate whether pain and itch induced by nonspecific TRPA1 agonists are reduced by treatment with TRPA1 inhibitors and to evaluate the effect of TRPA1 inhibition on pain and itch symptoms in patients with disease such as atopic dermatitis or chronic neuropathic pain. The efficacy of CGRP receptor antagonists for migraine at least confirms a role for neuropeptides released by sensory neurons in a chronic pain indication in humans (Vu et al., 2017).

In conclusion, *in vitro* experiments demonstrated that GDC-0334 is a very potent and highly selective TRPA1 inhibitor across multiple species that binds to the TRPA1 transmembrane domain, as per the cryoEM-elucidated structure. GDC-0334 inhibited TRPA1 HASMC contraction *in vitro*, and *in vivo* experiments demonstrated that GDC-0334 administered orally reduces airway inflammation, edema, and cough *in vivo* in preclinical species. Furthermore, GDC-0334 inhibited AITC-induced DBF, pain, and itch in healthy human subjects. Collectively, these results highlight a well-conserved role for TRPA1 in the fundamental regulation of inflammation across species and provide a scientific rationale for testing GDC-0334 in clinical studies to evaluate the efficacy of TRPA1 inhibition in asthma, as well as indications that feature inflammation, vascular leakage, pain, and itch.

Materials and methods

Animals

All animals used in preclinical experiments were housed under specific pathogen-free conditions until used in a study.

Experimental procedures involving animals were approved by Genentech's Institutional Animal Care and Use Committee. Hartley guinea pigs (6 wk old) were purchased from Charles River-Kingston. For AITC-induced blood perfusion, 5-wk-old female Hartley guinea pigs were purchased from Hilltop Lab Animals Inc. For all other guinea pig experiments, 5-wk-old female Hartley guinea pigs were purchased from Hilltop Lab Animals Inc. For OVA experiments, Brown Norway rats were purchased from Charles River Laboratories. For AITC-induced blood perfusion experiments, 3-mo-old female Sprague Dawley rats were purchased from Charles River Laboratories. For cough experiments, male Dunkin-Hartley guinea pigs (220–250 g) from Charles River Laboratories were ordered and quarantined for 14 d, and the experimental protocols were approved by the Institutional Animal Care and Use Committee at Lovelace Respiratory Research Institute. Animals used to evaluate PK in preclinical species are described separately (see PK in Preclinical species section).

Transgenic preclinical models

Slcn10a-cre^{+/-} mice were bred with *B6.DTR^{loxP/loxP}* mice to generate *Slcn10a-Dtr⁺* mice; littermates *Slcn10a-Dtr⁻* were used as control. *Trpa1^{loxP/loxP}* mice were bred with *Slcl7a6-cre^{+/-}* mice to generate *Trpa1^{fllox/fllox} Slcl7a6^{cre+}* mice; littermates *Slcl7a6^{cre-}* were used as control. *Slcl7a6-cre^{+/-}* mice were bred with *Rosa26.LSL.tdTomato* mice to generate *Slcl7a6-Tdt* mice. *Trpa1^{-/-}* mice were generated as a result of depleting human *Trpa1* cDNA from human Ki-conditional knockout (CKO) *Trpa1* mice. Homologous recombination and mouse embryonic stem (ES) cell technology (Kuehn et al., 1987; Smithies et al., 1985; Thomas et al., 1986) was used to generate a genetically modified mouse strain with a *Trpa1* CKO. A gene targeting vector constructed with a 2,997-bp arm of 5' homology corresponds to GRCm38/mm10 chr1: 14,922,295–14,919,299, and a 2,564-bp arm of 3' homology arm corresponds to chr1: 14,918,710–14,916,147. The 588-bp region flanked by loxP sites (untranslated region [UTR] plus exon1) corresponds to chr1: 14,919,298–14,918,711. The human cDNA (27 exons-[3,357 bp]) for the *Trpa1*-SV40-*frt-neo-frt-loxP* site was inserted after the ATG of mouse exon1 corresponded to chr1: 14,918,833–14,918,832. The rest of mouse exon 1 was deleted after the ATG plus 14 bp of intron to prevent donor splicing, and this corresponds to GRCm38/mm10 chr1: 14,918,832–14,918,711. The final vector was confirmed by DNA sequencing, linearized, and used to target C2 (C57BL/6N) ES cells using standard methods (G418-positive and ganciclovir-negative selection; Newman et al., 2015). C57BL/6N C2 ES cells (Gertsenstein et al., 2010) were electroporated with 20 μ g of linearized targeting vector DNA and cultured under drug selection. Targeted ES cells were subjected to karyotyping. Euploid gene-targeted ES cell clones were treated with Adeno-FLP to remove PGK neomycin, and ES cell clones that lacked PGK neomycin cassette were microinjected into albino BL/6N embryos. Germline transmission was obtained after crossing resulting chimeras with C57BL/6N females. Genomic DNA from pups was screened by long-range PCR to verify the desired gene-targeted structure of human Ki-CKO *Trpa1* before colony expansion.

Zygotes from heterozygous progeny carrying a CKO allele, in which human *Trpa1* cDNA is flanked by loxP sites, were incubated with HTN Cre to remove the floxed sequence. This led to a complete deletion of mouse *Trpa1* Exon1 including 14 intronic bp. Treated zygotes were transferred to pseudopregnant female mice to obtain *Trpa1*^{-/-} pups. Genotyping was performed using the following primers: common reverse primer 1, 5'-CTGAAG GTTGGGTAAGCA-3'; forward primer 2, 5'-AGGAGTGGACAA GAGAGA-3', and forward primer 3, 5'-AGAATACTGAACGAA AGGAAAT-3' amplified 140-bp wild-type, 174-bp loxP, and 166-bp knockout DNA fragments. *Trpa1*^{-/-} rats were generated as previously described (Reese et al., 2020).

TRPA1 in vitro pharmacology

Activity of GDC-0334 on TRPA1 was determined in a fluorescence-based Ca²⁺ assay as described previously (Chen et al., 2011). Briefly, cells expressing TRPA1 from various species were loaded with fluorescence Ca²⁺ dye, then incubated with varying concentrations of GDC-0334 for 10 min before a stimulation with the agonist CA. To account for the slight difference in CA sensitivity, half-maximal effective concentration (EC₈₀) of CA (i.e., 75 μM for human, 35 μM for cyno, 40 μM for rat, 11.1 μM for guinea pig, and 75 μM for dog TRPA1) was used to evoke Ca²⁺ responses, and the peak responses were used to derive concentration-dependent block. Similarly, activities of GDC-0334 on human TRPV1 and TRPM8 were determined in Ca²⁺ responses evoked by 30 nM capsaicin (~EC₈₀) and 50 μM menthol (~EC₈₀), respectively. Activity on human TRPC6 was determined in a membrane potential assay using 75 μM carbochol.

Calcium imaging

Calcium imaging experiments were conducted 15–24 h after plating. Cells were loaded with Fura-2AM ester (Molecular Probes) and placed in a perfusion chamber for recording using a Zeiss upright microscope. Ratiometric fluorescence measurements were made by measuring emission to sequential excitation at 340 and 380 nm, using a DG-4 wavelength switching system (Sutter Instrument Co.). Fluorescence data points were collected at 0.5 Hz using AxioVision software (Zeiss) and analyzed using Origin (OriginLab Corporation). During the recording, cells were continuously perfused with normal saline (155 mM NaCl, 2 mM KCl, 1 mM MgCl₂, 1.8 mM CaCl₂, 10 mM Hepes, pH 7.4, and 5 mM glucose). TRPA1 activity was measured by perfusing cells with saline containing 50 μM AITC (Sigma). Neurons in the field of observation were identified by their calcium influx response to 50 mM KCl-containing saline. Only neurons were included in the analysis. Responses to AITC were normalized to mean KCl response for each experiment.

TRP channel assays

Activity of GNE-0334 on TRPA1 was determined in a fluorometric imaging plate reader-based Ca²⁺ assay as described previously (Chen et al., 2011). Briefly, cells expressing TRPA1 from various species were loaded with fluorescence Ca²⁺ dye, then incubated with varying concentrations of GDC-0334 for 10 min before a stimulation with the agonist CA. To count for the slight

difference in CA sensitivity, EC₈₀ concentration of CA (i.e., 75 μM for human, 35 μM for cyno, 40 μM for rat, 11.1 μM for guinea pig, and 75 μM for dog TRPA1) was used to evoke Ca²⁺ responses, and the peak responses were used to derive concentration-dependent block. Similarly, activities of GNE-0334 on human TRPV1 and TRPM8 were determined in Ca²⁺ responses evoked by 30 nM capsaicin (~EC₈₀) and 50 μM menthol (~EC₈₀), respectively. Activity on human TRPC6 was determined in a membrane potential assay using 75 μM carbochol.

Processing and imaging of whole-mount tissue

Animals were anesthetized using isoflurane and perfused with PBS/Heparin (5 U/ml) followed by tissue fixation using paraformaldehyde 4% (Doerr et al., 2017). The tissue was harvested and subjected to immunolabeling using primary conjugated antibodies and a previously published staining protocol avoiding methanol treatment steps (Renier et al., 2014). Tissue clearing was performed using the FluoClearBABB approach (Schwarz et al., 2015), and whole-mount images were then acquired using a Leica SP8 microscope equipped with a white light laser and a Leica BABB immersion lens (HCX APO L 20×/0.95 immersion media). Acquired data were visualized on a power workstation using Imaris (Bitplane).

Generation of rabbit anti-TRPA1 mAbs

New Zealand White rabbits were immunized with rat TRPA1, and single B cells were isolated from peripheral blood mononuclear cells using a modified protocol related to published literature (Seeber et al., 2014). This modified workflow included direct FACS sorting of IgG⁺/TRPA1⁺ single B cells into 96 wells. The individual B cell culture supernatants were then assayed by ELISA for binding to rat TRPA1 protein and an irrelevant control protein. TRPA1-specific B cells were lysed and immediately frozen in -80°C for storage until molecular cloning. Variable regions (VH and VL) of each mAb from rabbit B cells were cloned into expression vectors from extracted mRNA as previously described (Seeber et al., 2014). Individual recombinant rabbit antibodies were expressed in Expi293 cells and subsequently purified with protein A. Purified anti-TRPA1 antibodies were then subjected to immunohistochemistry (IHC) screening.

IHC

IHC was performed using a rabbit monoclonal anti-TRPA1 antibody (clone Rb1.11D5; see Generation of rabbit anti-TRPA1 mAb). Formalin-fixed, paraffin-embedded mouse lung left lobe, nodose ganglia tissues, and cell pellets were treated with Target Antigen Retrieval Solution (Agilent Technologies). Primary antibodies were preincubated in 20% mouse serum (Jackson ImmunoResearch). Detection employed donkey anti-rabbit biotinylated secondary antibody (Jackson ImmunoResearch) followed by Streptavidin-HRP with tyramide signal amplification (PerkinElmer) and metal-enhanced diaminobenzidine visualization (Thermo Fisher Scientific). Slides were counterstained with Mayer's hematoxylin (Rowley Biochemical), cleared with xylene, and mounted with Tissue-Tek Glass synthetic mounting medium (Sakura).

Preparation of nodose ganglion and DRG cell suspensions

Nodose homogenate was obtained by pulling nodose ganglia from three mice. Mice were sacrificed in the morning by carbon dioxide inhalation followed by decapitation. After the ganglia were removed, the isolated ganglia were immediately transferred into a 24-well plate containing digestion solution (1 ml high glucose DMEM and 100 μ l Collagenase Type IV (Sigma; C1889-50 mg) and incubated at 37°C for 40 min. The nodose ganglia were then transferred to a well containing 1 ml HBSS and 100 μ l Trypsin (Sigma; T9935-50 mg) and were incubated 5 min at 37°C. After digestion, the nodose ganglia were gently washed three times with Hibernate A medium, preventing any tissue breakdown. The following trituration step was performed in 500 μ l of Hibernate A by using a 1-ml pipette (pipette up and down 10–15 times) followed by a 200- μ l pipette (pipette up and down 15–20 times). This procedure generated a cloudy solution containing dissociated cell suspension. DRG cell suspension was obtained following the same procedure used for the nodose ganglion, except DRGs were incubated in 1 ml HBSS containing 100 μ l Trypsin for 40 min at 37°C.

RNA isolation and quantitative real-time PCR

Total RNA was isolated from lung tissue or monolayer cells with an RNeasy Mini Kit (Qiagen). An ABI 7500 real-time RT-PCR system (Applied Biosystems) and TaqMan One-Step RT-PCR Master Mix (Applied Biosystems) were used for real-time RT-PCR (primers and probe sets from Applied Biosystems). Each sample was run in triplicate and normalized to the reference gene *b-actin* or *GAPDH*. Relative quantification was determined by the cycle threshold (CT) method. The TaqMan Gene Expression Assays included specific primers and FAM/MGB probes for mouse *Gapdh* (endogenous Control [4352932E]), mouse *Il5* (Mm00439646_m1), mouse *Trpa1* (Mm00625268_m1), rat *Trpa1* (Rn01473803_m1), guinea pig *Trpa1* (Cp04230147_m1), human *Tie2* (Hs00945150_m1), human *TRPA1* (Hs00175798_m1), human *MUC5AC* (Hs01365616_m1), and human *GAPDH* (Hs02786624_g1).

Fluorescence-activated cell sorting and quantitative real-time PCR

The cell suspensions derived from Advilin-Cre tdTomato mice were sorted on the BD FACSAria Fusion system (BD Biosciences) at low pressure, speed of 500 events/second using a 100- μ m nozzle. Calcein AM (Promokine; PK-CA707-80011-3) treatment at 1:1,000 dilution was used to identify live cells. High fluorescence-intensity TdTomato and green-fluorescent calcein-positive cells were sorted. Single sorted cells were directly collected into a MicroAmp Optical 96-well reaction plate (Life Technologies) containing 10 μ l lysis buffer. RNA underwent reverse transcription and cDNA preamplification according to the manufacturer's instructions (Ambion Single Cell to CT kit). Gene expression was assessed using *Trpa1* (Mm01227437_m1) and *Nav18* (Mm00501467_m1) Taqman probes (Thermo Fisher Scientific).

Experimental drug formulation

For oral dosing, GDC-0334 was formulated by dissolving the compound in DMSO first (15% of total target volume). After the

compound was completely dissolved in DMSO, MCT (0.6% methylcellulose/0.2% Tween 80, 85% of the target volume) was added to the solution. The compound precipitated as amorphous material upon MCT addition. Formulations used to evaluate PK in preclinical species are described separately (see PK in Pre-clinical species section).

Recombinant expression and purification of truncated human TRPA1

The encoding sequence for human *TRPA1* [Ser448-Thr1078] was synthesized (Genscript) and cloned into a modified pAcGP67A vector downstream of the polyhedron promoter. Recombinant baculovirus was generated using the Baculogold system (BD Biosciences) following standard protocols. *Trichoplusia ni* cells were infected for protein production and harvested 48 h after infection. The sequence of the construct for structural studies is shown below (the underlined sequence is the 6-His followed by an MBP affinity tag, the TEV protease cleavage site is in bold, and a (GGG)₄ linker shown in italic was added in-between the TEV cleavage sequence and *TRPA1* sequence): MHHHHHHGK IEEGKLVWINGDKGYNGLAIEVGGKFEKDTGKIVTVEHPDKLEEK FPQVAATGDGPDIIFWAHDREFGGYASQSGLLAEITPDKAFQDKLVP FTWDAVRYNGKLIAYPIAVEALSILIYNDLLPNPPKTWEEIPALD KELKAKGKSALMFNLQEPYFTWPLIADGGYAFKYENGGKYDI KDVGVNDAGAKAGLTFLVDLIKHKHMNADTDYSIAEAAFNGK ETAMTINGPWAWSNIDTSKVNYGVTVLPTFKGQPSKPFVGVLSAGINAASPNKELAKEFLENYLLTDEGLEAVNKDKPLGAVALKSY EEELAKDPRIAATMENAQKGEIMPNIQMSAFWYAVRTAVIN AASGRQTVDEALKDAQTNSSSSNNNNNNNNNNNGENLYFQGS GGGSGGGSGGSPHFSAASYGRINTCQRLLQDISDTRLLNEGDL HGMTPLHLAAKNGHDKVVQLLLKKGALFLSDHNGWTALHHS MGGYTQTMKVIDTDLNLDKCTDRLEDEGNTALHFAAREGHAKAV ALLSHNADIVLNKQASFLHLALHNKRKEVLTIRSKRWDECL KIFSHNSPGNKCPITEMIEYLPECMKVLLDFCMLHSTEDKSCRDY YIEYNFKYLQCPLEFTKKTPTQDVIYEPLTALNAMVQNNRIELN HPVCKEYLLMKWLAYGFRAHMMNLGSLYCLGLIPMTILVVNIK PGMFAFNSTGIINETS DHSEILDTTNSYLIKTCMILVFLSSIFGYC KEAGQIFQQRNYFMDISNVLEWIIYTTGIIFVLPFVPEIAPHLQ WQCGAIAVYFYWMNFLLYLQRFENCGIFIVMLEVILKTLRS TVVFIFLLAFGLSFYILLNLQDPFSSPLLSIIQTFSSMMLGDINRYES FLEPYLRNELAHPVLSFAQLVSFTIFVPIVLMNLLIGLAVGDIAD VQKHASKRIAMQVELHTSLEKLLPLWFLRQVDQKSTIVYYPN KPRSGGMLFHIFCFLFCTGEIRQEIPNADKSLEMEILKQKYRLKD LTFLEKQHELKLIQKMEISET.

250 g of harvested cell pellet was resuspended in lysis buffer (50 mM Tris, pH 7.5, 150 mM NaCl, 1 μ g/ml benzonase, 0.5 mM TCEP (tris[2-carboxyethyl]phosphine), and Roche Complete protease inhibitor tablets). Cells were homogenized, microfluidized once, and spun down at 8,000 g for 20 min and then spun down at 40,000 g for 60 min. Membranes were solubilized in 25 mM Tris, pH 8, 150 mM NaCl, 10% glycerol, 0.5 mM TCEP, Complete protease inhibitor tablets, and 1% (wt/vol) FA-3 (Avanti; Façade-EM) at 4°C for 2 h. Insoluble debris was pelleted by ultracentrifugation at 40,000 rpm for 60 min, and the supernatant containing the solubilized protein was collected for affinity purification by batch binding to 3 ml of amylose resin for 1 h at 4°C. Solution was then poured onto a

Bio-Rad column and repacked by gravity flow. The column was washed with 5 CV of 25 mM Tris, pH 8, 150 mM NaCl, and 0.5 mM TCEP with 0.06% FA-3 (Buffer A) and eluted with 3 CV of Buffer A + 40 mM maltose. The elution fraction was concentrated down to 400 μ l (~4 mg/ml) with 100-kD MWCO concentrators (Millipore Sigma; Amicon Ultra-15 Centrifugal Filter Units). Three-fold excess (wt/wt) of PMAL-C8 (Anatrace, 100 mg/ml stock solution in water) was added along with TEV protease (prepared in-house) and EndoF1 and EndoH deglycosidases (prepared in-house). A sample was nutated overnight at 4°C. Biobeads were added to the sample and incubated at 4°C for 2 h. Beads were filtered out, and supernatant was loaded onto a Superose 6 3.2/300 column linked to an AKTA system pre-equilibrated with 25 mM Tris, pH 8.2, 150 mM NaCl, and 0.5 mM TCEP. A sample from the most concentrated fraction (around 1 mg/ml) was incubated with 100 μ M of GDC-0334 (10 mM stock in 100% DMSO) at 4°C for 1 h and applied to grids.

CryoEM sample preparation and data acquisition

Holey carbon grids (C-flat, R2/1, Cu, 300 mesh) were plasma etched using a Solarus plasma cleaner (Gatan) in the hydrogen-oxygen setting for 5 min to thin the carbon foil. Each side was then coated with 6 nm of gold using an ACE600 plasma coater (Leica). Prior to sample application, the grid was glow-discharged in air at 0.67 mbar, with a current of 15 mA for 30 s in a GloQube (Quorum Technologies). A 3.5- μ l aliquot of the peak fraction was applied to the grid, which was then blotted twice, for 4 s each time, in a Vitrobot Mark IV (Thermo Fisher Scientific) operated with 100% relative humidity and a temperature of 4°C, and plunge-frozen in liquid ethane cooled by liquid nitrogen. Movie stacks were collected using SerialEM (Mastrorade, 2005) on a Titan Krios operated at 300 keV and equipped with a BioQuantum energy filter (operated with a slit width of 20 eV) and a K2 Summit direct electron detector (Gatan). Images were recorded at 130,000 nominal magnification corresponding to a calibrated pixel size of 1.085 Å. A total dose of 47.5 electrons/Å² was fractionated over 40 frames of 0.25 s each, corresponding to an exposure rate of 5.6 electrons per physical detector pixel per second.

CryoEM data processing

All image processing was performed with cisTEM (Grant et al., 2018) following the workflow depicted in Fig. S3. For atomic model building, Protein Data Bank accession no. 6PQQ (Suo et al., 2020) was rebuilt using interactive molecular dynamics in ISOLDE (Croll, 2018) and refined in real space using coot (Emsley et al., 2010). CryoEM structure statistics are described in Table S2.

Data and materials availability

The accession numbers for the cryoEM structure of TRPA1 bound by GDC-0334 are EMD-21688 at the Electron Microscopy Data Bank (map) and Protein Data Bank accession no. 6WJ5 (atomic model). The rest of the data are in the main text or in the supplemental materials.

Impedance-based assay by xCELLigence RTCA

Human primary bronchial smooth muscle cells (referred in the text as HASMCs) were obtained from Lonza. Human HASMCs

were cultured in SmGM-2 Medium supplemented with FBS, insulin, human (h)FGF-B, and hEGF at the concentrations suggested by the vendor (Lonza; SMG Bullet Kit #CC-3182). The bronchial smooth muscle cells were split every 3–4 d as they reached confluence and remained viable to use in experiments for up to five passages. Cell impedance assays were performed using the xCELLigence RTCA MP instrument and RTCA 2.0 software (ACEA Biosciences) as previously described (Bravo et al., 2018). HASMCs from an exponentially growing culture were seeded on a 96-well E-Plate (E-Plate VIEW 96) at a density of 10⁴ cells/well and incubated overnight. The following day, the cells were stimulated with TRPA1 agonists G00923551 (from Genentech). The cells were preincubated with appropriate antagonists for 1 h in full growth medium and then stimulated with relevant agonists. Cell impedance was recorded in the xCELLigence MP every 2 min for a period of 3 h immediately after the addition of the agonists. The impedance of electron flow caused by adherent cells is reported using a unitless parameter called cell index (CI), where CI = (impedance at time point *n* – impedance in the absence of cells)/nominal impedance value (<https://www.aceabio.com/products/rtca-mp>). For our impedance-based contraction experiment, the CI value of undisturbed cells was used as the baseline value (0% contraction). Then a concentration-dependent contractile stimulation curve was generated to determine the maximum contraction (defined as 100%) and EC₅₀ of a given agonist. For inhibition experiments, various concentrations of antagonists were preincubated with cells for 1 h, then challenged with EC₉₀ concentration of the contraction agonist. The CI values from the negative control (undisturbed cells) and positive control (agonist alone), defined as 0% and 100% of maximum contractility, were used to characterize each contraction antagonist.

In vitro ADME

Metabolic stability experiments

Metabolic stability experiments were performed with 1 μ M of compound and were evaluated in pooled cryopreserved hepatocytes (BioIVT) from female CD-1 mice, male Sprague Dawley rats, male beagle dogs, male cyno monkeys, and mixed gender humans using methods previously reported (Halladay et al., 2007). Cryopreserved hepatocytes were thawed and resuspended in DMEM (pH 7.4). An incubation mixture containing 0.5 \times 10⁶ cells/ml and 1 μ M compound was incubated in a 37°C incubator with 95% relative humidity and 5% CO₂ environment, and 50- μ l aliquots were sampled at 0, 60, 120, and 180 min and reaction quenched with 2 \times volume acetonitrile containing an in-house internal standard. Quenched samples from hepatocytes were centrifuged for 10 min at 2,000 *g*. Supernatant was removed and diluted with water (2 \times) and analyzed by liquid chromatography–tandem mass spectrometry using *t* = 0 and peak area ratio set to 100%. The in vitro intrinsic clearance and scaled hepatic clearance were determined as described by Obach et al. (1997).

MDCK permeability experiments

MDCK cells were plated in a 24-well plate at 2.5 \times 10⁵ cells/ml and allowed to grow for 4 d at 37°C in 95% humidity and 5% CO₂

environment. Media containing DMEM and Earle's balance salt solution supplemented with 10% FBS was changed 2 d after seeding and the day before the experiment. Compound was added to either the apical or the basolateral side of the monolayer at an initial concentration of 10 μM and was incubated at 37°C for 180 min. Samples were taken from the receiver chambers at 60, 120, and 180 min and analyzed by liquid chromatography–tandem mass spectrometry. The apparent permeability (P_{app}) in the apical-to-basolateral (A-B) and basolateral-to-apical (B-A) directions was calculated as $P_{\text{app}} = (dQ/dt) / (A \cdot C_0)$, where dQ/dt = rate of compound appearance in the receiver compartment; A = surface area of the insert; and C_0 = initial substrate concentration at time = 0. The efflux ratio was calculated as $(P_{\text{app, B-A}}/P_{\text{app, A-B}})$.

PK in preclinical species

Mouse PK

Six female CD-1 mice were obtained from Charles River Laboratory. All animals were 6–9 wk old at the time of study and weighed between 20 and 35 g. Animals ($n = 3$ per dosing route) were dosed with GDC-0334 at 0.5 mg/kg i.v. (in dimethyl sulfoxide [15% vol/vol], propyl ethylene glycol 400 [35% vol/vol], and saline [50% vol/vol]) or 1 mg/kg orally (suspended in 0.5% wt/vol methylcellulose, 0.2% wt/vol Tween 80). Food and water were available ad libitum to all animals. Serial blood samples (15 μl) were collected by tail nick at 0.033, 0.083, 0.25, 0.5, 1, 3, 8, and 24 h after the i.v. administration and 0.083, 0.25, 0.5, 1, 3, 8, and 24 h after the oral administration. All blood samples were diluted with 60 μl water containing 1.7 mg/ml EDTA and kept at -80°C until analysis.

Rat PK

12 male Sprague-Dawley rats were obtained from Charles River Laboratories. All animals were 6–9 wk old at the time of study and weighed between 200 and 300 g. Animals ($n = 3$ per dosing route) were dosed with GDC-0334 at 1 mg/kg i.v. (in dimethyl sulfoxide [15% vol/vol], propyl ethylene glycol 400 [60% vol/vol], and saline [25% vol/vol]) or 5 mg/kg orally (suspended in 0.5% wt/vol methylcellulose, 0.2% wt/vol Tween 80). Food and water were available ad libitum to animals in the i.v. groups. Animals in the oral groups were fasted overnight, and food was withheld until 4 h after dose. Approximately 250 μl of blood was collected via the catheter at 0.033, 0.083, 0.25, 0.5, 1, 2, 4, 8, and 24 h after the i.v. or oral administration. All blood samples were collected into tubes containing 5 μl of 0.5 M K_2EDTA and were processed for plasma. Samples were centrifuged (2,500 $\times g$ for 15 min at 4°C) within 1 h of collection, and plasma samples were kept at -80°C until analysis.

Dog PK

Six nonnaive male beagle dogs (>2 yr old at the time of study) were selected and weighed between 6 and 10 kg. Animals ($n = 3$ per dosing route) were dosed with GDC-0334 at 1 mg/kg i.v. (in dimethyl sulfoxide [10% vol/vol], propyl ethylene glycol 400 [60% vol/vol], and saline [30% vol/vol]) or 5 mg/kg orally (suspended in 0.5% wt/vol methylcellulose, 0.2% wt/vol Tween 80). Food and water were available ad libitum to animals in the

i.v. groups. Animals in the oral groups were fasted overnight, and food was withheld until 4 h after dose. Approximately 800 μl of blood was collected from a peripheral vessel at predose, 0.033, 0.083, 0.25, 0.5, 1, 3, 6, 9, and 24 h after the i.v. administration and predose, 0.083, 0.25, 0.5, 1, 3, 6, 9, and 24 h after the oral administration. All blood samples were collected into tubes containing 10 μl of 0.5 M K_2EDTA and were processed for plasma. Samples were centrifuged (3,000 $\times g$ for 10 min at 4°C) within 1 h of collection, and plasma samples were kept at -80°C until analysis.

Cyno monkey PK

Six nonnaive male cyno monkeys (>2 yr of age at time of study) were selected and weighed between 2 and 5 kg. Animals ($n = 3$ per dosing route) were dosed with GDC-0334 at 1 mg/kg i.v. (in dimethyl sulfoxide [10% vol/vol], propyl ethylene glycol 400 [60% vol/vol], and saline [30% vol/vol]) or 5 mg/kg orally (suspended in 0.5% wt/vol methylcellulose, 0.2% wt/vol Tween 80). Food and water were available ad libitum to animals in the i.v. groups. Animals in the oral groups were fasted overnight, and food was withheld until 4 h after dose. Approximately 800 μl of blood was collected from a peripheral vessel at predose, 0.033, 0.083, 0.25, 0.5, 1, 3, 6, 9, and 24 h after the i.v. administration and predose, 0.083, 0.25, 0.5, 1, 3, 6, 9, and 24 h after the oral administration. All blood samples were collected into tubes containing 10 μl of 0.5 M K_2EDTA and were processed for plasma. Samples were centrifuged (3,000 $\times g$ for 10 min at 4°C) within 1 h of collection, and plasma samples were kept at -80°C until analysis.

All animal studies were performed in accordance with the Guide for the Care and Use of Laboratory Animals as adopted and were approved by the institution's animal care and use committee. All PK parameters, clearance, half-life, and volume of distribution were calculated using Phoenix Winnolin.

Bioanalytical method of GDC-0334

Concentrations of GDC-0334 were determined by a nonvalidated HPLC–tandem mass spectrometry method. The plasma samples were prepared for analysis by placing a 25- μl aliquot into a 96-well plate followed by the addition of 200 μl of acetonitrile containing an internal standard mixture. The samples were vortexed and centrifuged at 4,000 rpm for 10 min at 4°C. 50 μl of the supernatant was diluted with 150 μl water and then injected onto an analytical column. A Shimadzu Nexera UHPLC system coupled to a QTRAP 5500 system (SCIEX) was used for sample analysis. The mobile phases were 0.1% of formic acid in water (A) and 0.1% of formic acid in acetonitrile (B). The gradient method (15–90% B) was used for chromatographic separation, and the total flow rate was 1.2 ml/min. Data were acquired using multiple reactions monitoring in positive ion electrospray mode. The multiple reactions monitoring transitions used were m/z 610.1 \rightarrow 260.1 for GDC-0334 and 477.1 \rightarrow 266.2 for loperamide as internal standard. A duplicate set of calibration curves was prepared using blank plasma with known concentrations of GDC-0334 (at least six levels) and was included in each HPLC–tandem mass spectrometry run of the study samples. The peak area ratio of the GDC-0334 to its corresponding internal

standard versus concentration of GDC-0334 was fit with a weighted quadratic curve or linear curve.

OVA challenge model of asthma in rodents

7–10-wk-old female mice of the appropriate genotype were sensitized by intraperitoneal injection of 100 μ l of 50 μ g of OVA (Biosearch Technologies, Inc.) mixed with 2 mg of alum (Thermo Fisher Scientific) in sterile PBS. 28 d after sensitization, mice were challenged daily for 30 min with an aerosolized solution of 1% OVA in PBS for 7 consecutive d for the efficacy model. 2 h before each OVA challenge, animals received either vehicle or GDC-0334 by gavage. Takedown was performed at day 35. After euthanasia, lungs were lavaged with 1.5 ml PBS. The BALF was centrifuged at 400 \times g for 10 min at 4°C to pellet the cell fraction, and the supernatant was stored at –80°C until the measurements of the cytokines and chemokine by Luminex. The cell pellet was resuspended in 1,000 μ l of cold PBS and was analyzed by FACS. The OVA model was performed as previously described when DT treatment was performed before OVA challenge. DT was injected intraperitoneally in *Dtr*⁺ and *Dtr*[–] mice each day for 7 consecutive d (200 ng DT in 100 μ l sterile PBS). DT injection resulted in controlled ablation of Nav1.8-lineage neurons. The increased insensitivity to pain associated with loss of Nav1.8-positive neurons can result in overgrooming behavior. Toenails of all animals were clipped using an appropriate sterile trimmer.

Rats were sensitized on day 0 with intraperitoneal administration of 150 μ g OVA mixed with 40 mg of alum diluted in sterile PBS. 28 d after sensitization, rats were challenged with 2% OVA in PBS aerosolized via a nebulizer for 30 min for 4 consecutive d. 3 h before each OVA challenge, animals received either vehicle or GDC-0334 by gavage. 24 h after the final treatment, rats were euthanized by CO₂ inhalation. After euthanasia, BALF was collected for total and differential cell counts by FACS. There were eight animals per group. Where indicated, 5 mg/kg Dexamethasone oral treatment, given at the same time as GDC-0334, was used as a positive control.

Hartley guinea pigs were immunized on day 0 and day 7 by intraperitoneal administration of 100 mg OVA mixed with 80 mg of alum diluted in sterile PBS. Animals then received an OVA challenge on day 28 by exposure to 0.1% OVA in PBS for 30 min via a nebulizer. 3 h before the OVA challenge, animals received either vehicle or GDC-0334 by gavage. 24 h after the OVA challenge, guinea pigs were euthanized via intraperitoneal injection of Euthasol. After euthanasia, blood was collected from the abdominal aorta for PK analysis. Lungs were lavaged and cells were collected for total and differential cell counts. There was a minimum of six animals per group.

Analysis of BALF

Lungs were lavaged with PBS. Bronchoalveolar lavage (BAL) cells were differentiated by microscopic analysis of methanol-fixed, Wright-Giemsa-stained cytospin slides or by flow cytometry. Red blood cells were lysed using ammonium-chloride potassium lysis buffer and washed with FACS buffer. For cytospin analysis, a microscopic review and manual differential leukocyte count (200 cells) were performed on all Wright-

Giemsa-stained BAL cytospin preparations by a blinded clinical pathology laboratory technologist. The percentages of eosinophils, neutrophils, monocytes, basophils, and lymphocytes were calculated and reported. Cell counts were determined by FACS analysis using a known quantity of Fluoresbrite yellow green microspheres (Polysciences) as a spike-in standard and Sitox blue as a stain for dead cells.

Flow cytometry of BAL cells was performed using the following antibody combination: mouse: CD45-FITC (553079), CD11cPe-cy7 (558079), CD11b BV421 (48-0112-82), MertK APC (151508), CD64 PE (558455), MHCII BV510 (562366), F4/80 Ax fluor 700 (123130), Ly6G BV605 (563005), SiglecF PE-CF594 (562757), and Fc Block (clone 2.4G2, BD Biosciences); rat: CD45 APC-Cy7 (202216), Cd11b FITC (554982), Granulocytes PE (550002), and RT1B AlexaFluor 647 (562223). Dead cells were excluded using the live/dead fixable aqua dead cell stain kit (Life Technologies) or sytox blue (Thermo Fisher Scientific).

Quantitative analysis of SP was performed in BALF supernatant. Neuropeptide levels were measured by enzyme immunoassay (Phoenix Pharmaceuticals).

Vascular permeability

NIRF

AITC-induced vascular permeability was measured in vivo by noninvasive NIRF of the rat ear. Rats were anesthetized by inhalation of isoflurane, injected with 100 μ l of the fluorescent blood pool dye Angiosense680 (PerkinElmer) via tail vein, and immediately placed into a Kodak 400 In-vivo FX Pro (Carestream Health) NIRF imaging system. The ear was immobilized to a glass window surface, preventing breathing artifacts. Body temperature was maintained at 37°C. Angiosense dye circulated for 5 min to equilibrate followed by topical application of 5% AITC (Sigma; #377430) dissolved in mineral oil to the left ear or 25 μ l mineral oil (vehicle) to the right ear. Images were collected at 1-min intervals immediately after probe injection for 20 min after AITC challenge (650-nm excitation/700-nm emission, 21.4 mm field of view, 10-s exposure, and 2 \times binning). A custom Matlab routine was designed to quantify changes in fluorescence intensity based on a region of interest positioned over the ear at each time point. Normalized changes in fluorescence were expressed as $\Delta F/F$, where absolute change in fluorescence (ΔF) was divided by the background magnitude of fluorescence.

Evans blue

Under isoflourane anesthesia, rats received an injection of 2% Evans blue dye (i.v., in saline, 2.5 ml/kg). Using a pipette, 25 μ l of 20% AITC solution was applied to one ear, and 25 μ l of mineral oil (vehicle) was applied to the contralateral ear immediately after Evans blue injection. For edema, ear thickness and plasma protein extravasation were assessed. For assessment of plasma protein extravasation, 20 min after AITC application Evans blue dye was extracted in formamide for 24 h at 65°C and quantified by 620-nm absorption on a spectrophotometer.

Preclinical LSCI

Rats were orally dosed 3 h before imaging with 0, 3.0, or 10.0 mg/kg GDC-0334 dissolved into 85% MCT and 15% DMSO.

Animals were anesthetized with isoflurane before and during imaging, and their body temperatures were maintained at 37°C using a feedback-controlled heating pad (Harvard Apparatus; model 507222F). To minimize breathing artifacts, rats were secured in ear bars (Kopf; model 900). LSCI (Moor Instruments; model moorFLPI-2) was used to monitor DBF in the rat ears. 13-min LSCI movies were acquired at 5 Hz with an 8.3-ms exposure time, 0.3-s time constant, and a 5 × 5-pixel spatial kernel size for calculating the speckle contrast. The rectangular imaging window was cropped to include both ears. 25 µl of mineral oil (left ear) and 25 µl of 5% AITC (Sigma; #377430) dissolved in mineral oil (right ear) were applied 1 min after imaging start. The animals were euthanized by CO₂ inhalation immediately after imaging, and blood samples were harvested into EDTA plasma collection tubes (BD; #365974) for PK analysis. The raw DBF traces were low-pass filtered at 0.3 Hz using the Matlab filtfilt function (Mathworks) to remove breathing artifacts. The traces were then normalized to fold-change by subtracting and dividing by the mean DBF value during the baseline period before AITC application.

The protocol for guinea pigs was the same as that used in rats with the following changes: the guinea pigs were orally dosed 3.5 h before imaging with 0, 5, 15, or 45 mg/kg GDC-0334. 15-min LSCI movies were acquired. 30 µl of mineral oil (left ear) and 30 µl of 25% AITC dissolved in mineral oil (right ear) were applied 1 min after imaging start. The animals were euthanized with Euthasol (Virbac; #710101) by intraperitoneal injection (1.5 ml/animal) immediately after imaging.

Cough studies

Dunkin-Hartley guinea pigs were fasted overnight. GDC-0334 at 35-, 75-, and 150-mg/kg dosages and its vehicle (15% DMSO in 85% MCT) were orally delivered in guinea pigs anesthetized with inhalation of isoflurane. 3 h later, they were individually placed in the chamber (Buxco) unrestrained with the bias air-flow rate 2.0 liter/minute (21% O₂ + 79% N₂, supplied by a gas mixing flowmeter). After stabilization of breathing for 5 min, the guinea pigs were exposed to 5 min aerosolized CA (25 mM), and they remained in the chamber for an additional 30 min. Respiratory activities, cough sound, and behavioral activities were continuously monitored and recorded online and analyzed later. For cough detection, a microphone system mounted in the roof of the plethysmography chamber was used to detect cough, while a video monitor placed outside of the chamber was used to monitor animal behavior. Animal respiratory activities were monitored and measured by a Buxco pneumotachograph transducer attached to the chamber. The number of coughs was counted by two trained observers.

Phase 1 human trial of GDC-0334

Study design

A Phase 1, double-blind, randomized, placebo-controlled, SAD study (ClinicalTrials.gov: NCT03381144, EUDRACT 2017-003498-33) was conducted at a single clinical site in the United Kingdom (Nottingham, UK) and was approved by the local review board. All subjects signed an informed consent form before participating in the study. SAD cohorts of healthy volunteers

were randomized in a 6 GDC-0334 to 2 placebo ratio to receive placebo or the following doses of GDC-0334 in a fasted condition: (A) 25 mg; (B) 75 mg; (C) 200 mg; and (D) 600 mg. The starting dose was designed to be submaximal for inhibition of the AITC-induced DBF based on results in guinea pigs and rats. Beginning with the starting dose of 25 mg, dose escalation between groups targeted exposure increase of approximately twofold to threefold and was determined following review of emerging safety and PK data collected up to 72 h after each dose. The primary outcome was to evaluate the safety and tolerability of a single oral dose of GDC-0334 in healthy subjects. The secondary outcome was to characterize the PK of a single oral dose of GDC-0334 in healthy subjects. Exploratory outcomes included assessment of the PD effect of GDC-0334 administered as a single oral dose to healthy subjects on DBF induced by topical application of the TRPA1 agonist AITC.

Subjects

All subjects were males and nonpregnant, nonlactating females aged 18–55 yr with body mass index of 18.0–32.0 kg/m² and deemed healthy as determined by medical history, 12-lead electrocardiogram (ECG), and vital signs. The median age of subjects was 34 yr (range, 26–51 yr) in the placebo group and 30 yr (range, 20–54 yr) in the GDC-0334 group. In the placebo group, a total of three male subjects (42.9%) and four female subjects (57.1%) were enrolled. In the GDC-0334 group, a higher number of female subjects (22 subjects [91.7%]) were enrolled compared with male subjects (two subjects [8.3%]). A majority of subjects were of white race in both placebo groups (six subjects [85.7%]) and GDC-0334 groups (22 subjects [91.7%]).

Key exclusion criteria

Subjects were excluded if they had received any investigational medicinal product in a clinical research study within the prior 3 mo. For the purposes of the PD AITC skin challenge assessment, subjects were excluded for the following reasons: history of serious adverse reaction or serious hypersensitivity to the challenge agent (AITC) or vehicle (mineral oil); presence or history of active allergy requiring treatment, as judged by the investigator; <100% DBF response during the screening skin challenge assessment; presence or history of dermatographism or clinically significant skin disorders, as judged by the investigator; history of trauma or surgery (laceration repair is not excluded) to the arm but not including wrist or hand injury/surgery; excessive tattoos, forearm hair, or other physical or behavioral characteristics that may interfere with PD objectives of the study, as determined and agreed by the principal investigator and sponsor.

Treatment assignment and blinding

Treatments were assigned using a computer-generated random allocation sequence by an unblinded study site statistician. Treatment assignments were not known by the subjects or clinical staff involved in the evaluation of the subjects and analysis of data except for the independent statistician, who generated the randomization list, and an unblinded site pharmacist, who maintained the randomization list to prepare and

dispense the study medication. Interim PK parameter estimations were performed with subject aliases to maintain the study blind until the study database was locked and the safety population defined.

GDC-0334 dosing

Subjects were provided with a light snack and then fasted from all food and drink (except water) for a minimum of 8 h on the day before dosing until ~4 h after dose, at which time lunch was provided. An evening meal was provided at ~10 h after dose and an evening snack at ~14 h after dose. On subsequent days, meals were provided at appropriate times. GDC-0334 or placebo was administered orally to subjects in a fasted state as 12.5- or 100-mg spray-dried dispersion tablets. 240 ml of water was given immediately following oral administration of the tablet.

Safety assessment and outcome measures

Sentinel dosing was implemented for all cohorts, where the first two subjects in each cohort were randomly assigned to receive either GDC-0334 or placebo, and the remaining subjects in the cohort were dosed at least 24 h after the last sentinel subject. Subjects were confined in a clinical research unit for 72 h after each dose and returned to the clinic for follow-up visits for up to 35 d after dosing. Safety assessments, in the form of repeated measures of vital signs, 12-lead ECGs, 24-h Holter ECG monitoring, physical and neurological examinations, and laboratory assessments, were performed before, during, and following each dose administration. Safety outcome measures included the nature, frequency, severity, and timing of TEAEs, including serious AEs and AEs of special interest. AEs of special interest were defined as cases of potential drug-induced liver injury as defined by Hy's Law (US Food and Drug Administration, 2009); suspected transmission of an infectious agent by the study drug; any serious hypersensitivity reaction or anaphylaxis; an injection-site reaction of Grade 2 or more; or an infection of Grade 3 or more.

PK outcome measures

Blood samples were collected before dose and at multiple time points after dose for the bioanalysis of GDC-0334. Human plasma concentrations of GDC-0334 were determined using validated analytical methods.

PD assessments and outcome measures

The PD effect of GDC-0334 on DBF, pain, and itch induced by topical application of AITC was evaluated as an exploratory outcome. The AITC skin challenge assay was performed during a screen visit and after dosing with GDC-0334 using methods previously described (Joseph et al., 2020). Briefly, 10% or 15% AITC (Sigma; catalog 377430) diluted in mineral oil was applied topically by pipette to four locations on the volar surface of the forearms, two each on the right and left forearms (Fig. 6 A). DBF was measured 2 min before and 21 min after AITC application by LSCI (Perimed). Subjects were asked to verbally indicate their pain and itch intensity using an interviewer-administered rating scale (0–10, with 0 being no pain/itch and 10 being the worst pain/itch imaginable) for the right and left arm at 2, 4, 6, 8, 10,

15, and 20 min after application of AITC. Subjects were required to experience $\geq 100\%$ increase in DBF relative to baseline during a screening AITC skin challenge assessment to enroll in the Phase 1 study. A washout period of at least 13 d between skin challenges on the same arm was required to allow residual redness or hyperpigmentation to subside before a second topical challenge on the same arm. The postdose AITC skin challenge assessment was performed at the approximate T_{max} , based on observations from preclinical species for cohort A (3 h after dose) and as determined following review of emerging PK data between dose groups (8 h after dose for cohort B and 6 h after dose for cohorts C and D).

Statistical methods

The sample size for this trial was based on the dose escalation rules and not on any statistical criteria. A sample size of eight subjects per regimen (to achieve six evaluable subjects) was expected to provide sufficient data to meet the primary objective.

DBF was quantified from the LSCI as previously described (Joseph et al., 2020). At each imaging visit, the DBF was normalized to baseline, averaged across the left and right arms, and summarized as change in DBF at 5, 10, and 15 min after baseline and into maximum and AUC between 0 and 10 min. The pain and itch were averaged across the left and right arms and summarized at 5, 10, and 15 min after baseline and into maximum between 0 and 20 min. The PD effect of GDC-0334 on the 20-min profile of AITC-induced DBF, pain, and itch between each dose group and pooled placebo groups was assessed using repeated-measures ANOVA using R. The DBF AUC from 0 to 10 min, maximal pain score, and maximal itch score for each dosing group were compared with those from a pooled placebo group by Dunnett's multiple comparison test using Graphpad Prism.

The PK parameters for GDC-0334 in plasma were estimated by noncompartmental analysis methods using Phoenix Win-Nonlin software (Certara USA, Inc.; v8.0). Dose proportionality was assessed using a power model. The relationship between DBF and PK was evaluated by nonlinear regression using Graphpad Prism. The safety objective was evaluated by descriptive summaries only.

Synthesis of GDC-0334

General methods

Unless otherwise indicated, all commercial reagents and anhydrous solvents were used without additional purification. $^1\text{H-NMR}$ spectra were measured on Bruker Avance III 300, 400, or 500 MHz spectrometers. $^{13}\text{C-NMR}$ spectra were measured on a Bruker Avance III 125.80 MHz spectrometer. Chemical shifts (in parts per million) were referenced to internal standard tetramethylsilane ($\delta = 0$ ppm). The reported carbon multiplicities and coupling constants are from C-F coupling. High-resolution mass spectrometry of final compounds was performed on a Thermo UHPLC/QE with a Thermo-Q Exactive mass spectrometry detector using ESI ionization, after elution on a Acquity BEH C18 (2.1 mm \times 50 mm; 1.7- μm particle size) stationary phase using a gradient of water/acetonitrile (3–97% over 7 min; 0.1%

formic acid in both phases). Reactions were monitored by walkup Shimadzu LCMS/UV system with LC-30AD solvent pump, 2020 MS, Sil-30AC autosampler, SPD-M30A UV detector, CTO-20A column oven, using 2–98% acetonitrile/0.1% formic acid (or 0.01% Ammonia) over 2.5 min OR Waters Acquity LCMS system using 2–98% acetonitrile/0.1% formic acid (or 0.1% Ammonia) over 2 min. Flash column chromatography purifications were done on a Teledyne Isco Combiflash Rf using Silicycle HP columns. Reverse-phase purification was performed on a Phenomenex Gemini-NX C18 (30 × 100 mm, 5 μm) with a gradient of 5–95% acetonitrile/water (with 0.1% formic acid or 0.1% NH₄OH) over 10 min at 60 ml/min.

(2-chloro-5-(trifluoromethyl)pyridin-4-yl)methanol (S2)

A solution of 2-chloro-5-(trifluoromethyl) pyridine-4-carboxylic acid (S1; 4.5 g, 19.95 mmol, 1.00 equiv) in tetrahydrofuran (40 ml) was added to a 250-ml three-necked round-bottom flask purged and maintained with an inert atmosphere of nitrogen, followed by the addition of BH₃.THF (1 M; 40 ml, 2.00 equiv) dropwise with stirring at 0°C over 10 min. The resulting solution was stirred at room temperature overnight, quenched by the addition of 10 ml of methanol at 0°C, concentrated under vacuum, and extracted with ethyl acetate. The combined organic layers were washed with brine, dried over sodium sulfate, and concentrated under vacuum. The residue was purified by a silica gel column eluted with ethyl acetate/petroleum ether (1:10) to afford 3 g (crude) of the title compound S2 as a white solid, which was used in the next reaction without further purification.

(5-(trifluoromethyl)-2-(2-(trifluoromethyl)pyrimidin-5-yl)pyridin-4-yl)methanol (S4)

(2-chloro-5-(trifluoromethyl)pyridin-4-yl)methanol (S2; 75.6 g, 357.33 mmol, 1.00 equiv), 1,4-dioxane (1.5 liter), 5-(tetramethyl-1,3,2-dioxaborolan-2-yl)-2-(trifluoromethyl)pyrimidine (S3; 110 g, 401.39 mmol, 1.20 equiv), K₂CO₃ (148 g, 1.06 mol, 3.00 equiv), and Pd(dppf)Cl₂ (13 g, 17.77 mmol, 0.05 equiv) were added to a 3-liter three-necked round-bottom flask purged and maintained with an inert atmosphere of nitrogen. The resulting solution was stirred at 100°C for 6 h under a nitrogen atmosphere, cooled to room temperature, and filtered. The filter cake was washed with 2 × 300 ml of ethyl acetate. The filtrate was then concentrated under vacuum, and the resulting residue was applied to a silica gel column eluted with ethyl acetate/petroleum ether (1/5–1/2) to afford 90 g (78%) of the title compound S4 as a white solid.

5-[4-(chloromethyl)-5-(trifluoromethyl)pyridin-2-yl]-2-(trifluoromethyl)pyrimidine (S5). A solution of [5-(trifluoromethyl)-2-[2-(trifluoromethyl)pyrimidin-5-yl]pyridin-4-yl]methanol (S4; 80 g, 247.53 mmol, 1.00 equiv) in tetrahydrofuran (800 ml) was added to a 2-liter three-necked round-bottom flask purged and maintained with an inert atmosphere of nitrogen, followed by the addition of LiHMDS (1 mol/liter; 322 ml, 1.30 equiv) dropwise with stirring at 0°C. The resulting mixture was then stirred at 0°C for 1 h. To this mixture was added 4-methylbenzene-1-sulfonyl chloride (61.2 g, 321.01 mmol, 1.30 equiv) in portions at 0°C under a nitrogen atmosphere. The

resulting solution was stirred from 0°C to 25°C for 24 h, cooled to 0°C, quenched by the addition of 100 ml of water, and extracted with 3 × 500 ml of ethyl acetate. The combined organic layers were dried over anhydrous sodium sulfate and concentrated under reduced pressure. The resulting residue was purified by silica gel column chromatography eluted with ethyl acetate/petroleum ether (1/10) to afford 30 g (35%) of the title compound S5 as a light yellow solid.

[5-(trifluoromethyl)-2-[2-(trifluoromethyl)pyrimidin-5-yl]pyridin-4-yl]methanamine hydrochloride (S6). A solution of 5-[4-(chloromethyl)-5-(trifluoromethyl)pyridin-2-yl]-2-(trifluoromethyl)pyrimidine (S5; 20 g, 58.54 mmol, 1.00 equiv) in methanol/NH₃ (140 ml) was added to a 200-ml sealed tube. The resulting solution was stirred at 80°C in an oil bath for 5 h. This reaction was twice repeated at the same scale. The reaction mixtures were then cooled to room temperature, combined, and concentrated under vacuum. The pH value of the aqueous solution was adjusted to 8 with saturated aqueous sodium bicarbonate. The resulting solution was then extracted with 3 × 300 ml of dichloromethane, and the combined organic layers were dried over anhydrous sodium sulfate and concentrated under vacuum. The residue was applied onto a silica gel column eluted with 10–30% ethyl acetate in petroleum ether to afford [5-(trifluoromethyl)-2-[2-(trifluoromethyl)pyrimidin-5-yl]pyridin-4-yl]methanamine 33 g as a light yellow solid. The residue was dissolved in 800 ml of ethyl acetate, and the product was precipitated by the addition of ethyl acetate/HCl (g). The resulting mixture was concentrated under vacuum. The solids were then collected by filtration, and the filter cake was subsequently washed with 3 × 2,500 ml of ether and dried to afford 31 g (49.5%) of the title compound S6 as a white solid. LCMS [M+H⁺] 323.

(2S,3R,5S)-tert-butyl 3-fluoro-2-methyl-5-((5-(trifluoromethyl)-2-(2-(trifluoromethyl)pyrimidin-5-yl)pyridin-4-yl)methyl)carbamoyl)pyrrolidine-1-carboxylate (S8). A mixture of (2S,4R,5S)-1-[(tert-butoxy)carbonyl]-4-fluoro-5-methylpyrrolidine-2-carboxylic acid (S7; 14 g, 56.62 mmol, 1.00 equiv), HATU (32 g, 84.16 mmol, 1.51 equiv), diisopropylethylamine (22 g, 170.22 mmol, 3.05 equiv), and [5-(trifluoromethyl)-2-[2-(trifluoromethyl)pyrimidin-5-yl]pyridin-4-yl]methanamine hydrochloride (S6; 20 g, 55.76 mmol, 1.00 equiv) in dimethylformamide (150 ml) was stirred for 2 h at room temperature. The resulting solution was diluted with ethyl acetate, washed with brine, dried over anhydrous sodium sulfate, and concentrated under vacuum. The residue was then purified by a silica gel column eluting with ethyl acetate/petroleum ether (1/1) to afford the title compound S8 (28 g, 91%) as a white solid. LCMS [M+H⁺] 552.

(2S,4R,5S)-4-fluoro-5-methyl-N-((5-(trifluoromethyl)-2-(2-(trifluoromethyl)pyrimidin-5-yl)pyridin-4-yl)methyl)pyrrolidine-2-carboxamide hydrochloride (S9). A mixture of tert-butyl (2S,3R,5S)-3-fluoro-2-methyl-5-(((5-(trifluoromethyl)-2-[2-(trifluoromethyl)pyrimidin-5-yl]pyridin-4-yl)methyl)carbamoyl)pyrrolidine-1-carboxylate (S8; 28 g, 50.77 mmol, 1.00 equiv) and saturated HCl (g) in 1,4-dioxane (200 ml) was stirred for 12 h at room temperature. The resulting mixture was concentrated under vacuum to afford the title compound S9 (22 g, 89%) as a white solid. LCMS [M+H⁺] 452.

(2S,4R,5S)-4-fluoro-1-(4-fluorophenylsulfonyl)-5-methyl-N-((5-(trifluoromethyl)-2-(2-(trifluoromethyl)pyrimidin-5-yl)pyridin-4-yl)methyl)pyrrolidine-2-carboxamide (GDC-0334, 1). A mixture of (2S,4R,5S)-4-fluoro-5-methyl-N-[[5-(trifluoromethyl)-2-(2-(trifluoromethyl)pyrimidin-5-yl)pyridin-4-yl]methyl]pyrrolidine-2-carboxamide hydrochloride (S9; 24.5 g, 50.22 mmol, 1.00 equiv), 4-fluorobenzene-1-sulfonyl chloride (20 g, 102.76 mmol, 2.00 equiv), and triethylamine (15 g, 148.23 mmol, 3.00 equiv) in dichloromethane (500 ml) was stirred for 2 h at room temperature. The resulting mixture was washed with brine, dried over anhydrous sodium sulfate, and concentrated under vacuum. The residue was purified by a silica gel column eluting with ethyl acetate/petroleum ether (1/1) to afford the title compound 1 (25 g, 82%) as a white solid. LCMS [M+H⁺] 610. ¹H NMR (400 MHz, CDCl₃) δ 9.70 (s, 2H), 9.01 (s, 1H), 8.38 (s, 1H), 7.94–7.91 (m, 2H), 7.40–7.38 (m, 1H), 7.30–7.26 (m, 1H), 5.24–5.18 (m, 1H), 4.81–4.68 (d, J = 51.2 Hz, 1H), 4.59–4.54 (m, 1H), 4.35–4.31 (m, 1H), 4.16–4.06 (m, 1H), 2.68–2.58 (m, 1H), and 1.41 (d, J = 7.2 Hz, 3H).

Study approval

Experimental procedures involving animals were approved by Genentech's Institutional Animal Care and Use Committee. The Phase 1 clinical study (ClinicalTrials.gov: NCT03381144, EU-DRACT 2017-003498-33) was approved by the local review board. All subjects signed an informed consent form before participating in the study.

Statistics and biological replicates

For preclinical data, selected figures were graphed and statistical analysis was performed using PRISM v6.0 software (GraphPad). Comparison of single treatments against control treatments was performed using two-tailed Student's *t* test with Welch's correction. Analysis of statistical differences comparing multiple treatments to each other or to a control treatment was performed via ordinary ANOVA with Dunnett's multiple comparison test with a single pooled variance. *P* value <0.05 was considered significant.

All in vivo experiments were repeated a minimum of two times. Since each biological replicate shows comparable trend and statistical significance among the sample groups, a representative graph of an individual experiment was chosen for the paper.

Online supplemental material

Fig. S1 shows calcium influx and TRPA1 gene expression in human, mouse, rat, and guinea pig primary cells. **Fig. S2** presents TRPA1 neuronal and nonneuronal contributions to OVA-induced airway inflammation in mice. **Fig. S3** shows cryoEM structure determination of human TRPA1–GDC-0334. **Fig. S4** provides GDC-0334 in vivo PK profiles and effect on the OVA-induced asthma model in rats and guinea pigs and the guinea pig model of cough. **Fig. S5** shows that GDC-0334 reduces AITC-induced perfusion and nocifensive behavior in rats and the itch and pain scores in humans. Table S1 lists GDC-0334 potency and selectivity, shows the mean IC₅₀ values of G03061334 in the Ca²⁺ assay for TRPM8, TRPV1, and TRPC6 channels, and lists the most commonly used TRPA1 tool antagonists for studying TRPA1 biology and companies of origin. Table S2 presents cryoEM structure statistics.

Acknowledgments

We thank Rajita Pappu, Menno van Lookeren Campagne, Joseph Arron, Rick Brown, Tracy Staton, and Liz Newton for critical input on the project; Lin Pan, Paula Belloni, Horace Rhee, Farah Gowgani, Joshana Amiel, Edward Cruz, Joshua Galanter, Chandra Chopra, Robby Weimer, Alex de Crespigny, and the staff at Quotient Clinical for support of the Phase 1 study; Tulika Tyagi, Scott Stawicki, and WeiYu Lin for purification of TRPA1 antibody; Ashley Cook with help on the BAL manual cell counts; Debra Dunlap for help with IHC; Charles Jones III and Ryan Pata for help with histology; Linda Bao for formulation of GDC-0334; the Department of Drug Metabolism and Pharmacokinetics for supporting the in vitro permeability and stability assessments; Robert Newman, microinjection, production, and genotyping group, for generating human Ki–CKO TRPA1 construct; and the biomolecular resources department at Genentech for support throughout the project.

This work was funded by Genentech, Inc.

Author contributions: A. Balestrini, J. Kortmann, J.E. Heredia, W.P. Lee, E. Suto, X. Wu, J. Liu, J. H., and J. Zhang performed OVA experiments and analysis. A. Balestrini, D.H. Hackos, M. Dourado, T. Chernov-Rogan, J. Wang, and J. Chen conducted and analyzed fluorescence-based calcium imaging and assay. R.M. Reese performed and analyzed rat experiments of nocifensive behavior. R.M. Reese and S.D. Shields conducted and analyzed AITC-induced skin edema in rats. D.D. Bravo performed and analyzed the impedance-based assay. C.D. Austin, C. Bjornson, L. Leong, and K. Hötzel performed and analyzed IHC imaging. B.M. Liederer oversaw the preclinical drug metabolism and pharmacokinetic studies of GDC-0334, and J. Liu, L. Chen, L. Liu, and J.Q. Ly performed the PK analysis. M. Volgraf, B.S. Safina, and S. Magnuson oversaw the chemical development of GDC-0334, and H. Chen, E. Villemure, D.G.M. Shore, V.A. Verma, B. Hu, L. Wang, and Y. Chen contributed to the design and synthesis of GDC-0334. K.H. Barck and R.A.D. Carano contributed to preclinical imaging studies. J. Payandeh designed TRPA1 constructs for structural studies. A. Estevez and C.P. Arthur conducted cryoEM experiments. L. Rougé, B. Brillantes, and C. Tam contributed to human TRPA1 purification for structural studies. M. Jung and J.A.V. Heiden performed computational analysis. A. Rohou, J. Payandeh, and C. Ciferri supervised structural studies. A. Rohou and C. Ciferri analyzed cryoEM data. V. Joseph, A. Gogineni, V. Gandham, and J. Elstrott conducted and analyzed preclinical laser speckle and near-infrared imaging studies. V. Joseph, X. Yang, S.S. Gao, H.T. Ding, J.H. Lin, and R.N. Bauer contributed to the design of the Phase 1 study and conducted analysis of the AITC skin challenge in human subjects. M. Roose-Girma and L. Tam designed the targeting vector and performed ES cell screening to generate *Trpa1*^{-/-} mice. A. Balestrini, R.L. Wong, and J. Doerr performed imaging acquisition of lung innervation. L. Riol-Blanco and B.S. Safina coordinated the research. A. Balestrini, M. Volgraf, A. Rohou., R.N. Bauer, and L. Riol-Blanco wrote the manuscript.

Submitted: 31 July 2020

Revised: 19 October 2020

Accepted: 23 December 2020

References

- Andr , E., B. Campi, S. Materazzi, M. Trevisani, S. Amadesi, D. Massi, C. Creminon, N. Vaksman, R. Nassini, M. Civelli, et al. 2008. Cigarette smoke-induced neurogenic inflammation is mediated by alpha,beta-unsaturated aldehydes and the TRPA1 receptor in rodents. *J. Clin. Invest.* 118:2574–2582.
- Aubdool, A.A., X. Kodji, N. Abdul-Kader, R. Heads, E.S. Fernandes, S. Bevan, and S.D. Brain. 2016. TRPA1 activation leads to neurogenic vasodilation: involvement of reactive oxygen nitrogen species in addition to CGRP and NO. *Br. J. Pharmacol.* 173:2419–2433. <https://doi.org/10.1111/bph.13519>
- Bai, T.R., D. Zhou, T. Weir, B. Walker, R. Hegele, S. Hayashi, K. McKay, G.P. Bondy, and T. Fong. 1995. Substance P (NK1)- and neurokinin A (NK2)-receptor gene expression in inflammatory airway diseases. *Am. J. Physiol.* 269:L309–L317. <https://doi.org/10.1152/ajplung.1995.269.3.L309>
- Baral, P., B.D. Umans, L. Li, A. Wallrapp, M. Bist, T. Kirschbaum, Y. Wei, Y. Zhou, V.K. Kuchroo, P.R. Burkett, et al. 2018. Nociceptor sensory neurons suppress neutrophil and $\gamma\delta$ T cell responses in bacterial lung infections and lethal pneumonia. *Nat. Med.* 24:417–426. <https://doi.org/10.1038/nm.4501>
- Bautista, D.M., M. Pellegrino, and M. Tsunozaki. 2013. TRPA1: A gatekeeper for inflammation. *Annu. Rev. Physiol.* 75:181–200. <https://doi.org/10.1146/annurev-physiol-030212-183811>
- Belvisi, M.G., and M.A. Birrell. 2017. The emerging role of transient receptor potential channels in chronic lung disease. *Eur. Respir. J.* 50:1601357. <https://doi.org/10.1183/13993003.01357-2016>
- Belvisi, M.G., M.A. Birrell, S. Khalid, M.A. Wortley, R. Dockry, J. Coote, K. Holt, E. Dubuis, A. Kelsall, S.A. Maher, et al. 2016. Neurophenotypes in Airway Diseases. Insights from Translational Cough Studies. *Am. J. Respir. Crit. Care Med.* 193:1364–1372. <https://doi.org/10.1164/rccm.201508-1602OC>
- Bessac, B.F., M. Sivula, C.A. von Hehn, J. Escalera, L. Cohn, and S.E. Jordt. 2008. TRPA1 is a major oxidant sensor in murine airway sensory neurons. *J. Clin. Invest.* 118:1899–1910. <https://doi.org/10.1172/JCI34192>
- Bessac, B.F., M. Sivula, C.A. von Hehn, A.I. Caceres, J. Escalera, and S.E. Jordt. 2009. Transient receptor potential ankyrin 1 antagonists block the noxious effects of toxic industrial isocyanates and tear gases. *FASEB J.* 23:1102–1114. <https://doi.org/10.1096/fj.08-117812>
- Bianchi, B.R., X.F. Zhang, R.M. Reilly, P.R. Kym, B.B. Yao, and J. Chen. 2012. Species comparison and pharmacological characterization of human, monkey, rat, and mouse TRPA1 channels. *J. Pharmacol. Exp. Ther.* 341:360–368. <https://doi.org/10.1124/jpet.111.189902>
- Braman, S.S. 2006. The global burden of asthma. *Chest* 130(1, Suppl):4S–12S. https://doi.org/10.1378/chest.130.1_suppl.4S
- Bravo, D.D., T. Chernov-Rogan, J. Chen, and J. Wang. 2018. An impedance-based cell contraction assay using human primary smooth muscle cells and fibroblasts. *J. Pharmacol. Toxicol. Methods.* 89:47–53. <https://doi.org/10.1016/j.vascn.2017.10.006>
- Burki, N.K., and L.Y. Lee. 2010. Mechanisms of dyspnea. *Chest* 138:1196–1201. <https://doi.org/10.1378/chest.10-0534>
- Burma, N.E., H. Leduc-Pessah, C.Y. Fan, and T. Trang. 2017. Animal models of chronic pain: Advances and challenges for clinical translation. *J. Neurosci. Res.* 95:1242–1256. <https://doi.org/10.1002/jnr.23768>
- Caceres, A.I., M. Brackmann, M.D. Elia, B.F. Bessac, D. del Camino, M. D'Amours, J.S. Witek, C.M. Fanger, J.A. Chong, N.J. Hayward, et al. 2009. A sensory neuronal ion channel essential for airway inflammation and hyperreactivity in asthma. *Proc. Natl. Acad. Sci. USA.* 106:9099–9104. <https://doi.org/10.1073/pnas.0900591106>
- Canning, B.J., and Y. Chou. 2008. Using guinea pigs in studies relevant to asthma and COPD. *Pulm. Pharmacol. Ther.* 21:702–720. <https://doi.org/10.1016/j.pupt.2008.01.004>
- Canning, B.J., A.B. Chang, D.C. Bolser, J.A. Smith, S.B. Mazzone, and L. McGarvey. CHEST Expert Cough Panel. 2014. Anatomy and neurophysiology of cough: CHEST Guideline and Expert Panel report. *Chest* 146:1633–1648. <https://doi.org/10.1378/chest.14-1481>
- Cardell, L.O., R. Uddman, and L. Edvinsson. 1994. Low plasma concentrations of VIP and elevated levels of other neuropeptides during exacerbations of asthma. *Eur. Respir. J.* 7:2169–2173. <https://doi.org/10.1183/09031936.94.07122169>
- Cardone, G., J.B. Heymann, and A.C. Steven. 2013. One number does not fit all: mapping local variations in resolution in cryo-EM reconstructions. *J. Struct. Biol.* 184:226–236. <https://doi.org/10.1016/j.jsb.2013.08.002>
- Chang, R.B., D.E. Strohlich, E.K. Williams, B.D. Umans, and S.D. Liberles. 2015. Vagal Sensory Neuron Subtypes that Differentially Control Breathing. *Cell* 161:622–633. <https://doi.org/10.1016/j.cell.2015.03.022>
- Chen, J., and D.H. Hackos. 2015. TRPA1 as a drug target--promise and challenges. *Naunyn Schmiedebergs Arch. Pharmacol.* 388:451–463. <https://doi.org/10.1007/s00210-015-1088-3>
- Chen, J., S.K. Joshi, S. DiDomenico, R.J. Perner, J.P. Mikusa, D.M. Gauvin, J.A. Segreti, P. Han, X.F. Zhang, W. Niforatos, et al. 2011. Selective blockade of TRPA1 channel attenuates pathological pain without altering noxious cold sensation or body temperature regulation. *Pain* 152:1165–1172. <https://doi.org/10.1016/j.pain.2011.01.049>
- Chen, H., M. Volgraf, S. Do, A. Kolesnikov, D.G. Shore, V.A. Verma, E. Villemure, L. Wang, Y. Chen, B. Hu, et al. 2018. Discovery of a Potent (4R,5S)-4-Fluoro-5-methylproline Sulfonamide Transient Receptor Potential Ankyrin 1 Antagonist and Its Methylene Phosphate Prodrug Guided by Molecular Modeling. *J. Med. Chem.* 61:3641–3659. <https://doi.org/10.1021/acs.jmedchem.8b00117>
- Chiu, I.M., C.A. von Hehn, and C.J. Woolf. 2012. Neurogenic inflammation and the peripheral nervous system in host defense and immunopathology. *Nat. Neurosci.* 15:1063–1067. <https://doi.org/10.1038/nn.3144>
- Chu, H.W., M. Kraft, J.E. Krause, M.D. Rex, and R.J. Martin. 2000. Substance P and its receptor neurokinin 1 expression in asthmatic airways. *J. Allergy Clin. Immunol.* 106:713–722. <https://doi.org/10.1067/mai.2000.109829>
- Cohn, L., J.A. Elias, and G.L. Chupp. 2004. Asthma: mechanisms of disease persistence and progression. *Annu. Rev. Immunol.* 22:789–815. <https://doi.org/10.1146/annurev.immunol.22.012703.104716>
- Corren, J., R.F. Lemanske, N.A. Hanania, P.E. Korenblat, M.V. Parsey, J.R. Arron, J.M. Harris, H. Scheerens, L.C. Wu, Z. Su, et al. 2011. Lebrikizumab treatment in adults with asthma. *N. Engl. J. Med.* 365:1088–1098. <https://doi.org/10.1056/NEJMoal106469>
- Croll, T.I. 2018. ISOLDE: a physically realistic environment for model building into low-resolution electron-density maps. *Acta Crystallogr. D Struct. Biol.* 74:519–530. <https://doi.org/10.1107/S2059798318002425>
- Devos, F.C., B. Boonen, Y.A. Alpizar, T. Maes, V. Hox, S. Seys, L. Pollaris, A. Liston, B. Nemery, K. Talavera, et al. 2016. Neuro-immune interactions in chemical-induced airway hyperreactivity. *Eur. Respir. J.* 48:380–392. <https://doi.org/10.1183/13993003.01778-2015>
- Doerr, J., M.K. Schwarz, D. Wiedermann, A. Leinhaas, A. Jakobs, F. Schloen, I. Schwarz, M. Diedenhofen, N.C. Braun, P. Koch, et al. 2017. Whole-brain 3D mapping of human neural transplant innervation. *Nat. Commun.* 8:14162. <https://doi.org/10.1038/ncomms14162>
- Drake, M.G., G.D. Scott, E.D. Blum, K.M. Lebold, Z. Nie, J.J. Lee, A.D. Fryer, R.W. Costello, and D.B. Jacoby. 2018. Eosinophils increase airway sensory nerve density in mice and in human asthma. *Sci. Transl. Med.* 10:eaar8477. <https://doi.org/10.1126/scitranslmed.aar8477>
- Emsley, P., B. Lohkamp, W.G. Scott, and K. Cowtan. 2010. Features and development of Coot. *Acta Crystallogr. D Biol. Crystallogr.* 66:486–501. <https://doi.org/10.1107/S0907444910007493>
- Fahy, J.V. 2015. Type 2 inflammation in asthma--present in most, absent in many. *Nat. Rev. Immunol.* 15:57–65. <https://doi.org/10.1038/nri3786>
- Fahy, J.V., H.H. Wong, P. Geppetti, J.M. Reis, S.C. Harris, D.B. Maclean, J.A. Nadel, and H.A. Boushey. 1995. Effect of an NK1 receptor antagonist (CP-99,994) on hypertonic saline-induced bronchoconstriction and cough in male asthmatic subjects. *Am. J. Respir. Crit. Care Med.* 152:879–884. <https://doi.org/10.1164/ajrccm.152.3.7663799>
- Fischer, A., G.P. McGregor, A. Saria, B. Philippin, and W. Kummer. 1996. Induction of tachykinin gene and peptide expression in guinea pig nodose primary afferent neurons by allergic airway inflammation. *J. Clin. Invest.* 98:2284–2291. <https://doi.org/10.1172/JCI119039>
- Galli, S.J., and M. Tsai. 2012. IgE and mast cells in allergic disease. *Nat. Med.* 18:693–704. <https://doi.org/10.1038/nm.2755>
- Gallo, V., F.N. Dijk, J.W. Holloway, S.M. Ring, G.H. Koppelman, D.S. Postma, D.P. Strachan, R. Granell, J.C. de Jongste, V.W. Jaddoe, et al. 2017. TRPA1 gene polymorphisms and childhood asthma. *Pediatr. Allergy Immunol.* 28:191–198. <https://doi.org/10.1111/pai.12673>
- Gao, Y., E. Cao, D. Julius, and Y. Cheng. 2016. TRPV1 structures in nanodiscs reveal mechanisms of ligand and lipid action. *Nature* 534:347–351. <https://doi.org/10.1038/nature17964>
- Gertsenstein, M., L.M. Nutter, T. Reid, M. Pereira, W.L. Stanford, J. Rossant, and A. Nagy. 2010. Efficient generation of germ line transmitting chimeras from C57BL/6N ES cells by aggregation with outbred host embryos. *PLoS One.* 5:e11260. <https://doi.org/10.1371/journal.pone.0011260>
- Grace, M.S., M. Baxter, E. Dubuis, M.A. Birrell, and M.G. Belvisi. 2014. Transient receptor potential (TRP) channels in the airway: role in airway disease. *Br. J. Pharmacol.* 171:2593–2607. <https://doi.org/10.1111/bph.12538>
- Grant, T., A. Rohou, and N. Grigorieff. 2018. cisTEM, user-friendly software for single-particle image processing. *eLife.* 7:e35383. <https://doi.org/10.7554/eLife.35383>

- Green, D.P., N. Limjunyawong, N. Gour, P. Pundir, and X. Dong. 2019. A Mast-Cell-Specific Receptor Mediates Neurogenic Inflammation and Pain. *Neuron*. 101:412–420.e3. <https://doi.org/10.1016/j.neuron.2019.01.012>
- Halladay, J.S., S. Wong, S.M. Jaffer, A.K. Sinhababu, and S.C. Khojasteh-Bakht. 2007. Metabolic stability screen for drug discovery using cassette analysis and column switching. *Drug Metab. Lett.* 1:67–72. <https://doi.org/10.2174/18723120779814364>
- Hanania, N.A., S. Wenzel, K. Rosén, H.J. Hsieh, S. Mosesova, D.F. Choy, P. Lal, J.R. Arron, J.M. Harris, and W. Busse. 2013. Exploring the effects of omalizumab in allergic asthma: an analysis of biomarkers in the EXTRA study. *Am. J. Respir. Crit. Care Med.* 187:804–811. <https://doi.org/10.1164/rccm.201208-1414OC>
- Heber, S., M. Gold-Binder, C.I. Ciotu, M. Witek, N. Ninidze, H.G. Kress, and M.J.M. Fischer. 2019. A Human TRPA1-Specific Pain Model. *J. Neurosci.* 39:3845–3855. <https://doi.org/10.1523/JNEUROSCI.3048-18.2019>
- Hjerling-Leffler, J., M. Alqatari, P. Ernfor, and M. Koltzenburg. 2007. Emergence of functional sensory subtypes as defined by transient receptor potential channel expression. *J. Neurosci.* 27:2435–2443. <https://doi.org/10.1523/JNEUROSCI.5614-06.2007>
- Hondoh, A., Y. Ishida, S. Ugawa, T. Ueda, Y. Shibata, T. Yamada, M. Shikano, S. Murakami, and S. Shimada. 2010. Distinct expression of cold receptors (TRPM8 and TRPA1) in the rat nodose-petrosal ganglion complex. *Brain Res.* 1319:60–69. <https://doi.org/10.1016/j.brainres.2010.01.016>
- Hox, V., J.A. Vanoirbeek, Y.A. Alpizar, S. Voedisch, I. Callebaut, S. Bobic, A. Sharify, V. De Vooght, L. Van Gerven, F. Devos, et al. 2013. Crucial role of transient receptor potential ankyrin 1 and mast cells in induction of nonallergic airway hyperreactivity in mice. *Am. J. Respir. Crit. Care Med.* 187:486–493. <https://doi.org/10.1164/rccm.201208-1358OC>
- Joos, G., R. Pauwels, and M. van der Straeten. 1987. Effect of inhaled substance P and neurokinin A on the airways of normal and asthmatic subjects. *Thorax*. 42:779–783. <https://doi.org/10.1136/thx.42.10.779>
- Joos, G.F., W. Vincken, R. Louis, V.J. Schelfhout, J.H. Wang, M.J. Shaw, G.D. Cioppa, and R.A. Pauwels. 2004. Dual tachykinin NK1/NK2 antagonist DNK333 inhibits neurokinin A-induced bronchoconstriction in asthma patients. *Eur. Respir. J.* 23:76–81. <https://doi.org/10.1183/09031936.03.00101902>
- Jordt, S.E., D.M. Bautista, H.H. Chuang, D.D. McKemy, P.M. Zygmunt, E.D. Högestätt, I.D. Meng, and D. Julius. 2004. Mustard oils and cannabinoids excite sensory nerve fibres through the TRP channel ANKTM1. *Nature*. 427:260–265. <https://doi.org/10.1038/nature02282>
- Joseph, V., X. Yang, S.S. Gao, J. Elstrott, R.M. Weimer, W. Theess, C. Thrasher, N. Singh, J. Lin, and R.N. Bauer. 2020. Development of AITC-induced dermal blood flow as a translational in vivo biomarker of TRPA1 activity in human and rodent skin. *Br. J. Clin. Pharmacol.* <https://doi.org/10.1111/bcp.14370>
- Kay, A.B., F.R. Ali, L.G. Heaney, F. Benyahia, C.P.C. Soh, H. Renz, T.H. Lee, and M. Larché. 2007. Airway expression of calcitonin gene-related peptide in T-cell peptide-induced late asthmatic reactions in atopics. *Allergy*. 62:495–503. <https://doi.org/10.1111/j.1398-9995.2007.01342.x>
- Khalid, S., R. Murdoch, A. Newlands, K. Smart, A. Kelsall, K. Holt, R. Dockry, A. Woodcock, and J.A. Smith. 2014. Transient receptor potential vanilloid 1 (TRPV1) antagonism in patients with refractory chronic cough: a double-blind randomized controlled trial. *J. Allergy Clin. Immunol.* 134:56–62. <https://doi.org/10.1016/j.jaci.2014.01.038>
- Klionsky, L., R. Tamir, B. Gao, W. Wang, D.C. Immke, N. Nishimura, and N.R. Gavva. 2007. Species-specific pharmacology of Trichloro(sulfanyl)ethyl benzamides as transient receptor potential ankyrin 1 (TRPA1) antagonists. *Mol. Pain*. 3:39. <https://doi.org/10.1186/1744-8069-3-39>
- Koskela, H.O., L. Hyvärinen, J.D. Brannan, H.K. Chan, and S.D. Anderson. 2004. Coughing during mannitol challenge is associated with asthma. *Chest*. 125:1985–1992. <https://doi.org/10.1378/chest.125.6.1985>
- Koskela, H.O., M.K. Purokivi, K.M. Kontra, A.H. Taivainen, and H.O. Tuukiainen. 2008. Hypertonic saline cough provocation test with salbutamol pretreatment: evidence for sensorineural dysfunction in asthma. *Clin. Exp. Allergy*. 38:1100–1107. <https://doi.org/10.1111/j.1365-2222.2008.02996.x>
- Kuehn, M.R., A. Bradley, E.J. Robertson, and M.J. Evans. 1987. A potential animal model for Lesch-Nyhan syndrome through introduction of HPRT mutations into mice. *Nature*. 326:295–298. <https://doi.org/10.1038/326295a0>
- Liu, F., Z. Zhang, A. Levit, J. Levring, K.K. Touhara, B.K. Shoichet, and J. Chen. 2019. Structural identification of a hotspot on CFTR for potentiation. *Science*. 364:1184–1188. <https://doi.org/10.1126/science.aaw7611>
- Maddox, L., and D.A. Schwartz. 2002. The pathophysiology of asthma. *Annu. Rev. Med.* 53:477–498. <https://doi.org/10.1146/annurev.med.53.082901.103921>
- Maher, S.A., E.D. Dubuis, and M.G. Belvisi. 2011. G-protein coupled receptors regulating cough. *Curr. Opin. Pharmacol.* 11:248–253. <https://doi.org/10.1016/j.coph.2011.06.005>
- Mastronarde, D.N. 2005. Automated electron microscope tomography using robust prediction of specimen movements. *J. Struct. Biol.* 152:36–51. <https://doi.org/10.1016/j.jsb.2005.07.007>
- Mazzone, S.B., and B.J. Undem. 2016. Vagal Afferent Innervation of the Airways in Health and Disease. *Physiol. Rev.* 96:975–1024. <https://doi.org/10.1152/physrev.00039.2015>
- Moran, M.M. 2018. TRP Channels as Potential Drug Targets. *Annu. Rev. Pharmacol. Toxicol.* 58:309–330. <https://doi.org/10.1146/annurev-pharmtox-010617-052832>
- Mostafa, G.A., S.M. Reda, M.M. Abd El-Aziz, and S.A. Ahmed. 2008. Sputum neurokinin A in Egyptian asthmatic children and adolescents: relation to exacerbation severity. *Allergy*. 63:1244–1247. <https://doi.org/10.1111/j.1398-9995.2008.01784.x>
- Nagatomo, K., and Y. Kubo. 2008. Caffeine activates mouse TRPA1 channels but suppresses human TRPA1 channels. *Proc. Natl. Acad. Sci. USA*. 105:17373–17378. <https://doi.org/10.1073/pnas.0809769105>
- Nassenstein, C., K. Kwong, T. Taylor-Clark, M. Kollarik, D.M. Macglashan, A. Braun, and B.J. Undem. 2008. Expression and function of the ion channel TRPA1 in vagal afferent nerves innervating mouse lungs. *J. Physiol.* 586:1595–1604. <https://doi.org/10.1113/jphysiol.2007.148379>
- Nassini, R., P. Pedretti, N. Moretto, C. Fusi, C. Carnini, F. Facchinetti, A.R. Viscomi, A.R. Pisanò, S. Stokesberry, C. Brunmark, et al. 2012. Transient receptor potential ankyrin 1 channel localized to non-neuronal airway cells promotes non-neurogenic inflammation. *PLoS One*. 7:e42454. <https://doi.org/10.1371/journal.pone.0042454>
- Newman, R.J., M. Roose-Girma, and S. Warming. 2015. Efficient conditional knockout targeting vector construction using co-selection BAC recombineering (CoSBR). *Nucleic Acids Res.* 43:e124. <https://doi.org/10.1093/nar/gkv600>
- Nyman, E., B. Franzén, A. Nolting, G. Klement, G. Liu, M. Nilsson, A. Rosén, C. Björk, D. Weigelt, P. Wollberg, et al. 2013. In vitro pharmacological characterization of a novel TRPA1 antagonist and proof of mechanism in a human dental pulp model. *J. Pain Res.* 6:59–70. <https://doi.org/10.2147/JPR.S37567>
- Obach, R.S., J.G. Baxter, T.E. Liston, B.M. Silber, B.C. Jones, F. MacIntyre, D.J. Rance, and P. Wastall. 1997. The prediction of human pharmacokinetic parameters from preclinical and in vitro metabolism data. *J. Pharmacol. Exp. Ther.* 283:46–58.
- Ordovas-Montanes, J., S. Rakoff-Nahoum, S. Huang, L. Riol-Blanco, O. Barreiro, and U.H. von Andrian. 2015. The Regulation of Immunological Processes by Peripheral Neurons in Homeostasis and Disease. *Trends Immunol.* 36:578–604. <https://doi.org/10.1016/j.it.2015.08.007>
- Ortega, H.G., M.C. Liu, I.D. Pavord, G.G. Brusselle, J.M. FitzGerald, A. Chetta, M. Humbert, L.E. Katz, O.N. Keene, S.W. Yancey, and P. Chanez. MENSA Investigators. 2014. Mepolizumab treatment in patients with severe eosinophilic asthma. *N. Engl. J. Med.* 371:1198–1207. <https://doi.org/10.1056/NEJMoa1403290>
- Ortega, H.G., S.W. Yancey, B. Mayer, N.B. Gunsoy, O.N. Keene, E.R. Bleecker, C.E. Brightling, and I.D. Pavord. 2016. Severe eosinophilic asthma treated with mepolizumab stratified by baseline eosinophil thresholds: a secondary analysis of the DREAM and MENSA studies. *Lancet Respir. Med.* 4:549–556. [https://doi.org/10.1016/S2213-2600\(16\)30031-5](https://doi.org/10.1016/S2213-2600(16)30031-5)
- Paulsen, C.E., J.P. Armache, Y. Gao, Y. Cheng, and D. Julius. 2015. Structure of the TRPA1 ion channel suggests regulatory mechanisms. *Nature*. 525:552. <https://doi.org/10.1038/nature14871>
- Rabe, K.F., P. Nair, G. Brusselle, J.F. Maspero, M. Castro, L. Sher, H. Zhu, J.D. Hamilton, B.N. Swanson, A. Khan, et al. 2018. Efficacy and Safety of Dupilumab in Glucocorticoid-Dependent Severe Asthma. *N. Engl. J. Med.* 378:2475–2485. <https://doi.org/10.1056/NEJMoa1804093>
- Reese, R.M., M. Dourado, K. Anderson, S. Warming, K.L. Stark, A. Balestrini, E. Suto, W. Lee, L. Riol-Blanco, S.D. Shields, and D.H. Hackos. 2020. Behavioral characterization of a CRISPR-generated TRPA1 knockout rat in models of pain, itch, and asthma. *Sci. Rep.* 10:979. <https://doi.org/10.1038/s41598-020-57936-5>
- Renier, N., Z. Wu, D.J. Simon, J. Yang, P. Ariel, and M. Tessier-Lavigne. 2014. iDISCO: a simple, rapid method to immunolabel large tissue samples for volume imaging. *Cell*. 159:896–910. <https://doi.org/10.1016/j.cell.2014.10.010>
- Riol-Blanco, L., J. Ordovas-Montanes, M. Perro, E. Naval, A. Thiriot, D. Alvarez, S. Paust, J.N. Wood, and U.H. von Andrian. 2014. Nociceptive sensory neurons drive interleukin-23-mediated psoriasisiform skin inflammation. *Nature*. 510:157–161. <https://doi.org/10.1038/nature13199>

- Rostock, C., K. Schrenk-Siemens, J. Pohle, and J. Siemens. 2018. Human vs. Mouse Nociceptors - Similarities and Differences. *Neuroscience*. 387: 13-27. <https://doi.org/10.1016/j.neuroscience.2017.11.047>
- Satia, I., N. Tsamandouras, K. Holt, H. Badri, M. Woodhead, K. Ogungbenro, T.W. Felton, P.M. O'Byrne, S.J. Fowler, and J.A. Smith. 2017. Capsaicin-evoked cough responses in asthmatic patients: Evidence for airway neuronal dysfunction. *J. Allergy Clin. Immunol.* 139:771-779.e10. <https://doi.org/10.1016/j.jaci.2016.04.045>
- Satia, I., R. Watson, T. Scime, R.J. Dockry, S. Sen, J.W. Ford, P.D. Mitchell, S.J. Fowler, G.M. Gauvreau, P.M. O'Byrne, and J.A. Smith. 2019. Allergen challenge increases capsaicin-evoked cough responses in patients with allergic asthma. *J. Allergy Clin. Immunol.* 144:788-795.e1. <https://doi.org/10.1016/j.jaci.2018.11.050>
- Schellhout, V., R. Louis, W. Lenz, R. Heyrman, R. Pauwels, and G. Joos. 2006. The triple neurokinin-receptor antagonist CS-003 inhibits neurokinin A-induced bronchoconstriction in patients with asthma. *Pulm. Pharmacol. Ther.* 19:413-418. <https://doi.org/10.1016/j.pupt.2005.10.007>
- Schenkel, L.B., P.R. Olivieri, A.A. Boezio, H.L. Deak, R. Emkey, R.F. Graceffa, H. Gunaydin, A. Guzman-Perez, J.H. Lee, Y. Teffera, et al. 2016. Optimization of a Novel Quinazolinone-Based Series of Transient Receptor Potential A1 (TRPA1) Antagonists Demonstrating Potent in Vivo Activity. *J. Med. Chem.* 59:2794-2809. <https://doi.org/10.1021/acs.jmedchem.6b00039>
- Schwarz, M.K., A. Scherbarth, R. Sprengel, J. Engelhardt, P. Theer, and G. Giese. 2015. Fluorescent-protein stabilization and high-resolution imaging of cleared, intact mouse brains. *PLoS One*. 10:e0124650. <https://doi.org/10.1371/journal.pone.0124650>
- Seeber, S., F. Ros, I. Thorey, G. Tiefenthaler, K. Kaluza, V. Lifke, J.A.A. Fischer, S. Klostermann, J. Endl, E. Kopetzki, et al. 2014. A robust high throughput platform to generate functional recombinant monoclonal antibodies using rabbit B cells from peripheral blood. *PLoS One*. 9: e86184. <https://doi.org/10.1371/journal.pone.0086184>
- Skerratt, S. 2017. Recent Progress in the Discovery and Development of TRPA1 Modulators. *Prog. Med. Chem.* 56:81-115. <https://doi.org/10.1016/bs.pmch.2016.11.003>
- Smith, J.A. 2010. Interrupting the cough reflex in asthma. *Curr. Opin. Allergy Clin. Immunol.* 10:77-81. <https://doi.org/10.1097/ACI.0b013e328334e75f>
- Smithies, O., R.G. Gregg, S.S. Boggs, M.A. Koralewski, and R.S. Kucherlapati. 1985. Insertion of DNA sequences into the human chromosomal beta-globin locus by homologous recombination. *Nature*. 317:230-234. <https://doi.org/10.1038/317230a0>
- Staton, T.L., D.F. Choy, and J.R. Arron. 2016. Biomarkers in the clinical development of asthma therapies. *Biomarkers Med.* 10:165-176. <https://doi.org/10.2217/bmm.15.116>
- Story, G.M., A.M. Peier, A.J. Reeve, S.R. Eid, J. Mosbacher, T.R. Hricik, T.J. Earley, A.C. Hergarden, D.A. Andersson, S.W. Hwang, et al. 2003. ANKTM1, a TRP-like channel expressed in nociceptive neurons, is activated by cold temperatures. *Cell*. 112:819-829. [https://doi.org/10.1016/S0092-8674\(03\)00158-2](https://doi.org/10.1016/S0092-8674(03)00158-2)
- Suo, Y., Z. Wang, L. Zubcevic, A.L. Hsu, Q. He, M.J. Borgnia, R.R. Ji, and S.Y. Lee. 2020. Structural Insights into Electrophile Irritant Sensing by the Human TRPA1 Channel. *Neuron*. 105:882-894.e5. <https://doi.org/10.1016/j.neuron.2019.11.023>
- Talbot, S., R.E. Abdulnour, P.R. Burkett, S. Lee, S.J. Cronin, M.A. Pascal, C. Laedermann, S.L. Foster, J.V. Tran, N. Lai, et al. 2015. Silencing Nociceptor Neurons Reduces Allergic Airway Inflammation. *Neuron*. 87: 341-354. <https://doi.org/10.1016/j.neuron.2015.06.007>
- Thomas, K.R., K.R. Folger, and M.R. Capecchi. 1986. High frequency targeting of genes to specific sites in the mammalian genome. *Cell*. 44:419-428. [https://doi.org/10.1016/0092-8674\(86\)90463-0](https://doi.org/10.1016/0092-8674(86)90463-0)
- Tomaki, M., M. Ichinose, M. Miura, Y. Hirayama, H. Yamauchi, N. Nakajima, and K. Shirato. 1995. Elevated substance P content in induced sputum from patients with asthma and patients with chronic bronchitis. *Am. J. Respir. Crit. Care Med.* 151:613-617. https://doi.org/10.1164/ajrccm.151.3.Pt_1.613
- US Food and Drug Administration. 2009. Drug-Induced Liver Injury: Pre-marketing Clinical Evaluation. <https://www.fda.gov/downloads/Guidances/UCM174090.pdf> (accessed February 29, 2016)
- Van Schoor, J., G.F. Joos, B.L. Chasson, R.J. Brouard, and R.A. Pauwels. 1998. The effect of the NK2 tachykinin receptor antagonist SR 48968 (saredutant) on neurokinin A-induced bronchoconstriction in asthmatics. *Eur. Respir. J.* 12:17-23. <https://doi.org/10.1183/09031936.98.12010017>
- Vauquelin, G., and A. Packeu. 2009. Ligands, their receptors and ... plasma membranes. *Mol. Cell. Endocrinol.* 311:1-10. <https://doi.org/10.1016/j.mce.2009.07.022>
- Viana, F. 2016. TRPA1 channels: molecular sentinels of cellular stress and tissue damage. *J. Physiol.* 594:4151-4169. <https://doi.org/10.1113/JP270935>
- Virk, H.S., M.Z. Rekas, M.S. Biddle, A.K.A. Wright, J. Sousa, C.A. Weston, L. Chachi, K.M. Roach, and P. Bradding. 2019. Validation of antibodies for the specific detection of human TRPA1. *Sci. Rep.* 9:18500. <https://doi.org/10.1038/s41598-019-55133-7>
- Vu, T., P. Ma, J.S. Chen, J. de Hoon, A. Van Hecken, L. Yan, L.S. Wu, L. Hamilton, and G. Vargas. 2017. Pharmacokinetic-Pharmacodynamic Relationship of Erenumab (AMG 334) and Capsaicin-Induced Dermal Blood Flow in Healthy and Migraine Subjects. *Pharm. Res.* 34:1784-1795. <https://doi.org/10.1007/s11095-017-2183-6>
- Woodruff, P.G., B. Modrek, D.F. Choy, G. Jia, A.R. Abbas, A. Ellwanger, L.L. Koth, J.R. Arron, and J.V. Fahy. 2009. T-helper type 2-driven inflammation defines major subphenotypes of asthma. *Am. J. Respir. Crit. Care Med.* 180:388-395. <https://doi.org/10.1164/rccm.200903-0392OC>
- Yu, S., and A. Ouyang. 2009. TRPA1 in bradykinin-induced mechanical hypersensitivity of vagal C fibers in guinea pig esophagus. *Am. J. Physiol. Gastrointest. Liver Physiol.* 296:G255-G265. <https://doi.org/10.1152/ajpgi.90530.2008>
- Zhao, J., J.V. Lin King, C.E. Paulsen, Y. Cheng, and D. Julius. 2020. Irritant-evoked activation and calcium modulation of the TRPA1 receptor. *Nature*. 585:141-145. <https://doi.org/10.1038/s41586-020-2480-9>

Supplemental material

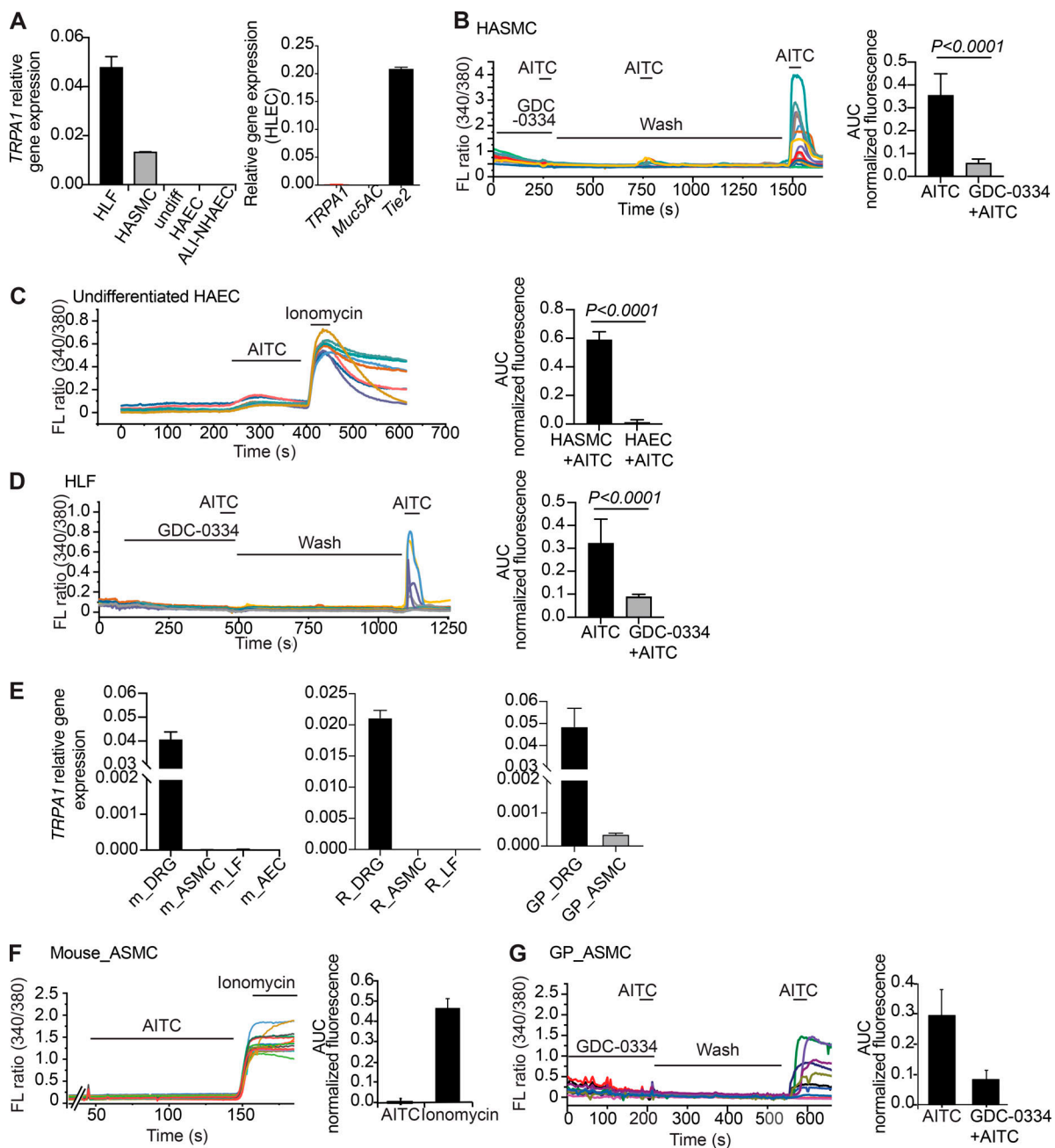


Figure S1. **Calcium influx and TRPA1 gene expression in human, mouse, rat, and guinea pig primary cells.** **(A)** Relative TRPA1 mRNA amounts were measured by Taqman Real-Time PCR assay in primary HASMCs, HLFs, HAECs, air-liquid interface of normal HAECs (ALI-NHAECs), and human lung endothelial cells (HLECs) from healthy volunteers. Results are normalized to the reference gene *GAPDH*. **(B–D)** Functional calcium imaging responses to the TRPA1 agonist AITC cultured with or without GDC-0334 from HASMCs (B), undifferentiated (Undiff) HAECs (C), and HLFs (D). Graphs to the right of the traces represent normalized AUC (two-tailed unpaired *t* test). Data are expressed as the mean \pm SD. **(E)** Relative *Trpa1* mRNA amounts were measured by Taqman Real-Time PCR assay from primary mouse DRGs (m-DRGs), mouse lung fibroblast (m-LFs), mouse ASM cells (m-ASMCs), undifferentiated mouse airway epithelial cells (m-AECs), rat DRGs (R-DRGs), ASM cells (R-ASMCs) and lung fibroblasts (R-LFs), and guinea pig DRGs (GP-DRGs), and guinea pig ASM cells (GP-ASMCs). Results are normalized to the reference gene *b-actin* or *Gapdh*. **(F)** Functional calcium imaging responses to the TRPA1 agonist AITC cultured from m-ASMCs. Ionomycin treatment was used as positive control for calcium influx. Graph to the right of the traces represents normalized AUC (two-tailed unpaired *t* test). Data are expressed as the mean \pm SD. **(G)** Functional calcium imaging responses to the TRPA1 agonist AITC cultured in guinea pig ASM cells. Graph to the right of the traces represents normalized AUC. Data are expressed as the mean \pm SD.

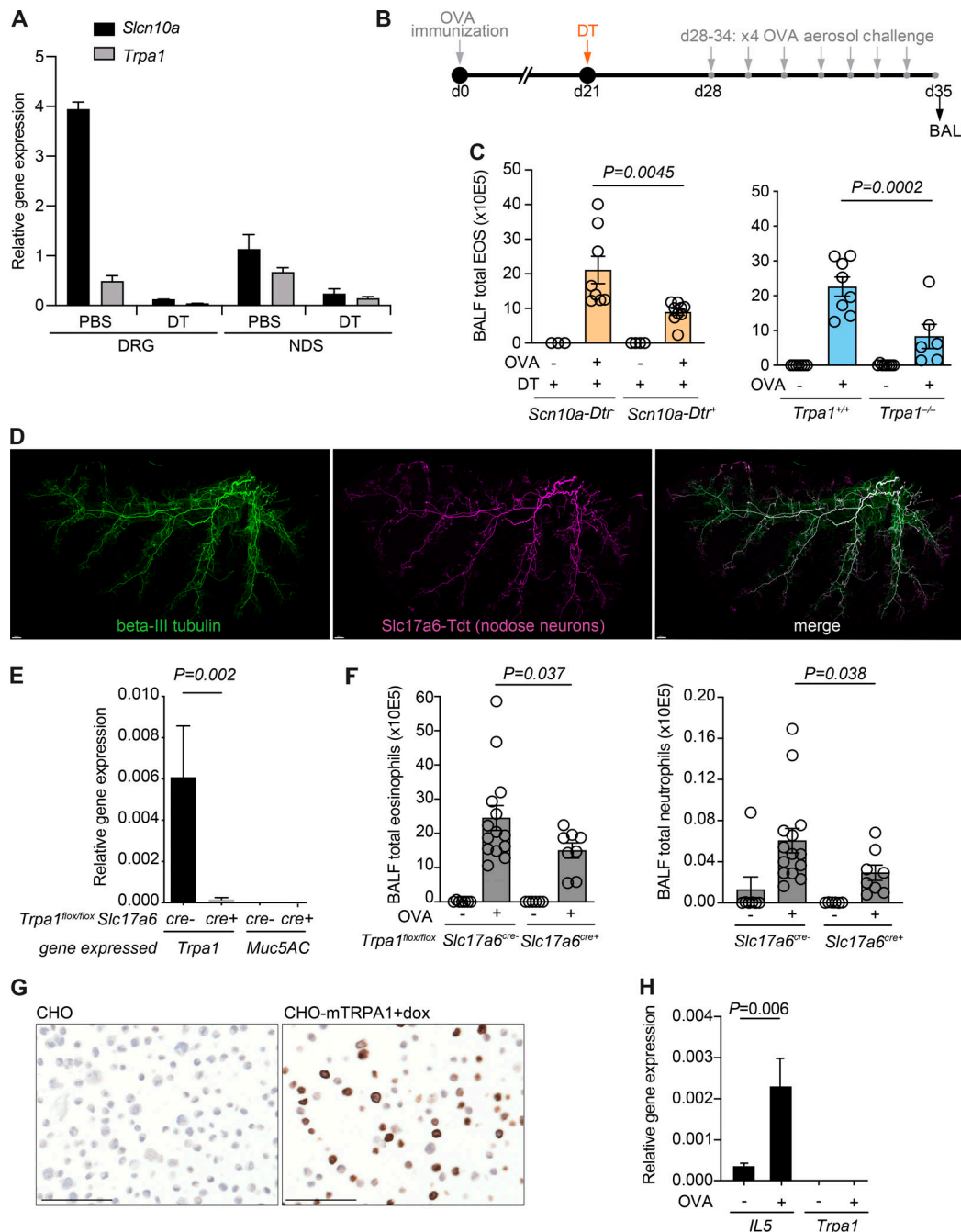


Figure S2. **TRPA1 neuronal and nonneuronal contributions to OVA-induced airway inflammation in mice.** (A) *Trpa1* and *Nav1.8* gene expression in nodose ganglion (NDS) and DRG after ablation of *Nav1.8*-expressing sensory neurons with DT. Error bars represent SEM; $n = 3$ animals per group. (B) Schematic outline of OVA challenge and DT treatment. (C) Analysis of leukocyte infiltration in the BALF of OVA-challenged mice. Eosinophil (EOS) cell counts from mice ablated of *Nav1.8*-expressing sensory neurons with DT (*Scn10a-DTR⁺*) or not (*Scn10a-DTR⁻*) and *Trpa1^{+/+}* versus *Trpa1^{-/-}* mice. Error bars represent SEM; $n \geq 8$ animals per group. A comparison for each pair was performed using one-way ANOVA. (D) Whole-mount staining for β -III tubulin (green) and tdTomato (Tdt; pink) fluorescence in a flattened lung left lobe from a *Vglut2 Cre* mouse. Scale bar = 500 μ m. (E) Total RNA extracted from primary mouse nodose ganglion of *Trpa1^{fllox/fllox} Slc17a6^{cre+}* and *Trpa1^{fllox/fllox} Slc17a6^{cre-}*. Relative *Trpa1* mRNA amounts were measured by Taqman Real-Time PCR assay. Results are normalized to the reference gene *b-actin*. Expression of *Muc5AC* gene was used as negative control. Error bars represent SEM; $n \geq 3$ animals per group. A comparison for each pair was performed using two-tailed *t* test. (F) Analysis of leukocyte infiltration in the BALF of OVA-challenged mice: eosinophil (left) and neutrophil (right) cell counts from mice depleted or not of neuronal TRPA1 (*Trpa1^{fllox/fllox} Slc17a6^{cre+}* or *Trpa1^{fllox/fllox} Slc17a6^{cre-}*, respectively). Error bars represent SEM; $n \geq 8$ animals per group. A comparison for each pair was performed using two-tailed *t* test. (G) Representative images of TRPA1 immunostaining show intense staining in doxycycline (dox)-induced mouse TRPA1-expressing CHO cells (CHO-mTRPA1+dox) and nodose ganglion from mouse *Trpa1^{+/+}*. No staining is detected in the absence of doxycycline (CHO) used as negative control. Scale bar = 100 μ m. (H) Increased lung *IL5* transcription in *Trpa1^{+/+}* OVA-challenged mice treated was determined by Taqman quantitative PCR. In the same samples, no *Trpa1* gene expression was detected. *B-actin* transcript levels were used for normalization as endogenous control. Animal groups OVA- (naive): $n = 7$; OVA+: $n = 8$. Error bars represent SEM; animal groups OVA- (naive): $n = 7$; OVA+: $n = 8$. A comparison for each pair was performed using two-tailed *t* test.

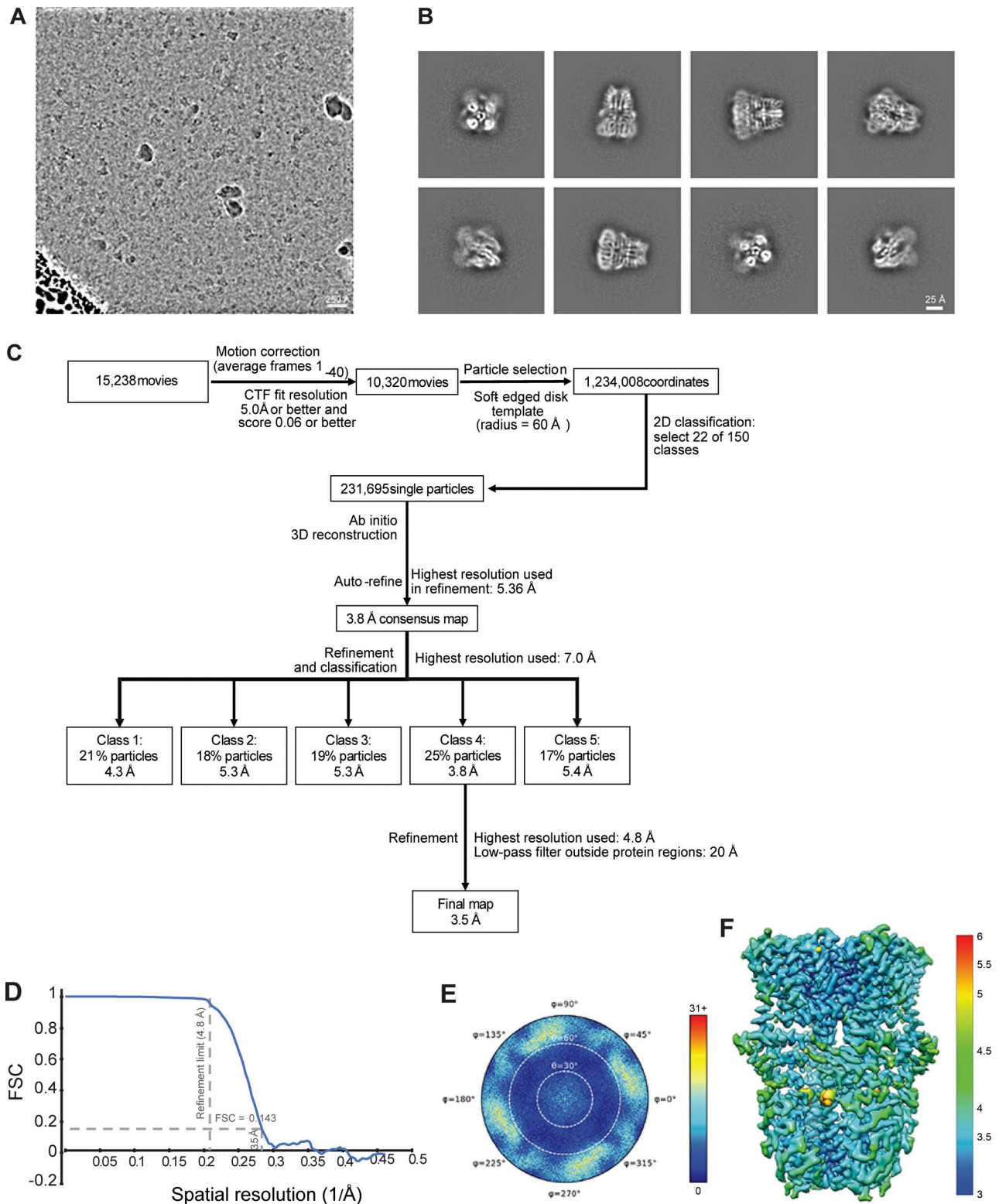


Figure S3. **CryoEM structure determination of human TRPA1-GDC-0334.** (A) Representative micrograph. (B) Representative class averages. (C) Single-particle image processing workflow. (D) Fourier Shell Correlation (FSC) between two half datasets yields a global resolution estimate of ~ 3.6 Å. No spatial frequencies beyond $1/4.8$ Å⁻¹ were used at any point during refinement. CTF, contrast transfer function. (E) Heat map representation of the distribution of assigned particle orientations shows a bias toward side views (near the periphery of the plot). (F) Isosurface rendering of the three-dimensional map with surface coloring according to the local resolution estimated by windowed FSCs (Cardone et al., 2013).

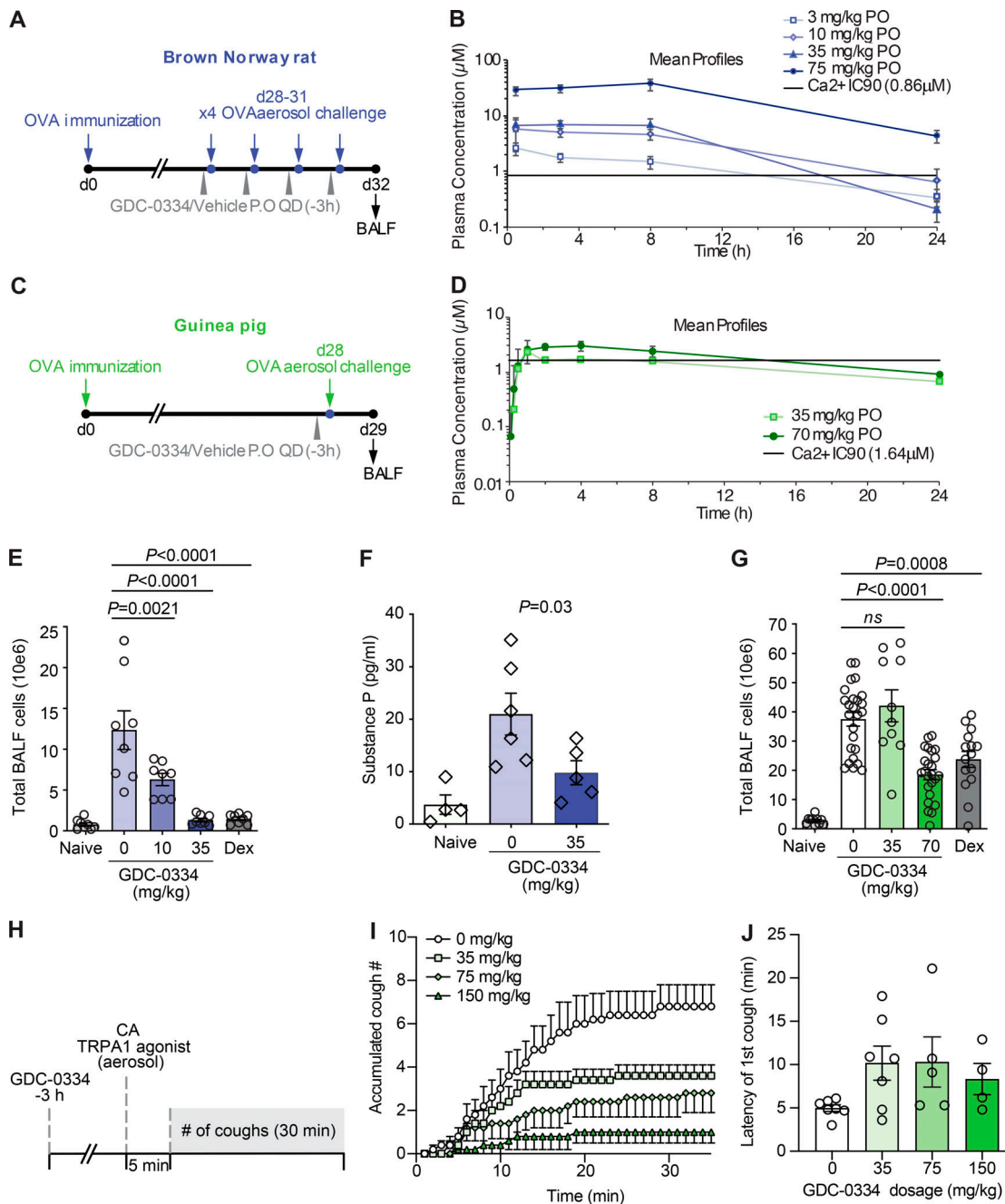


Figure S4. GDC-0334 in vivo PK profiles and effect on OVA-induced asthma model in rats and guinea pigs and guinea pig model of cough. (A) Design of rat OVA asthma model. Brown Norway rats were sensitized or not (naive group) and challenged with OVA. Animals received either GDC-0334 or vehicle via oral delivery 3 h before OVA challenge. 24 h after the final OVA challenge (32 d after initial OVA sensitization), BALF was analyzed by FACS for eosinophils and neutrophils. (B) Plasma concentrations of GDC-0334 following 3, 10, 35, or 70 mg/kg oral administration to rats. The black line indicates IC₉₀ value for GDC-0334 as determined in the Ca²⁺ influx cell-based assay and corrected for plasma protein binding. Mean and SD of three to six animals per group are shown. (C) Design of guinea pig OVA asthma model. Animals received either GDC-0334 or vehicle via oral delivery 3 h before OVA challenge. An unimmunized, unchallenged group was also included (naive). BALF was collected 24 h after the challenge for analysis of eosinophils and neutrophils. In both, A and B dexamethasone (Dex) was used as positive control. (D) Plasma concentrations of GDC-0334 following a single 35- or 70-mg/kg oral administration to guinea pigs. The black line indicates IC₉₀ value as determined in the Ca²⁺ influx cell-based assay and corrected for plasma protein binding. Mean and SD of three to six animals per group are shown. (E and G) Analysis of total cell infiltration in the BALF of OVA-challenged rats (E) and guinea pigs (F). Error bars represent SEM; n = 4–6 animals per group. Comparison for each pair was performed using one-way ANOVA. (F) Analysis of SP level in BALF of naive and OVA-challenged rats (vehicle and GDC-0334 treated). Error bars represent SEM; n = 5–8 animals per group. Comparison for each pair was performed using one-way ANOVA. (H) Experimental outline of the cough model. Guinea pigs were dosed with GDC-0334 3 h before treatment with 25 mM aerosolized CA. 5 min after CA treatment, the number of coughs was continuously assessed over a period of 30 min. (I) Accumulated cough numbers in individual animals in response to CA in guinea pigs pretreated with GDC-0334 at dosages of 0, 35, 75, and 150 mg/kg. Data are expressed as the mean \pm SEM. (J) Effect of oral gavage of vehicle (Veh) and indicated doses of GDC-0334 on cough latency (first cough after initiation of aerosol exposure of CA). Error bars represent SEM; n = 5–8 animals per group. PO, oral; QD, once a day.

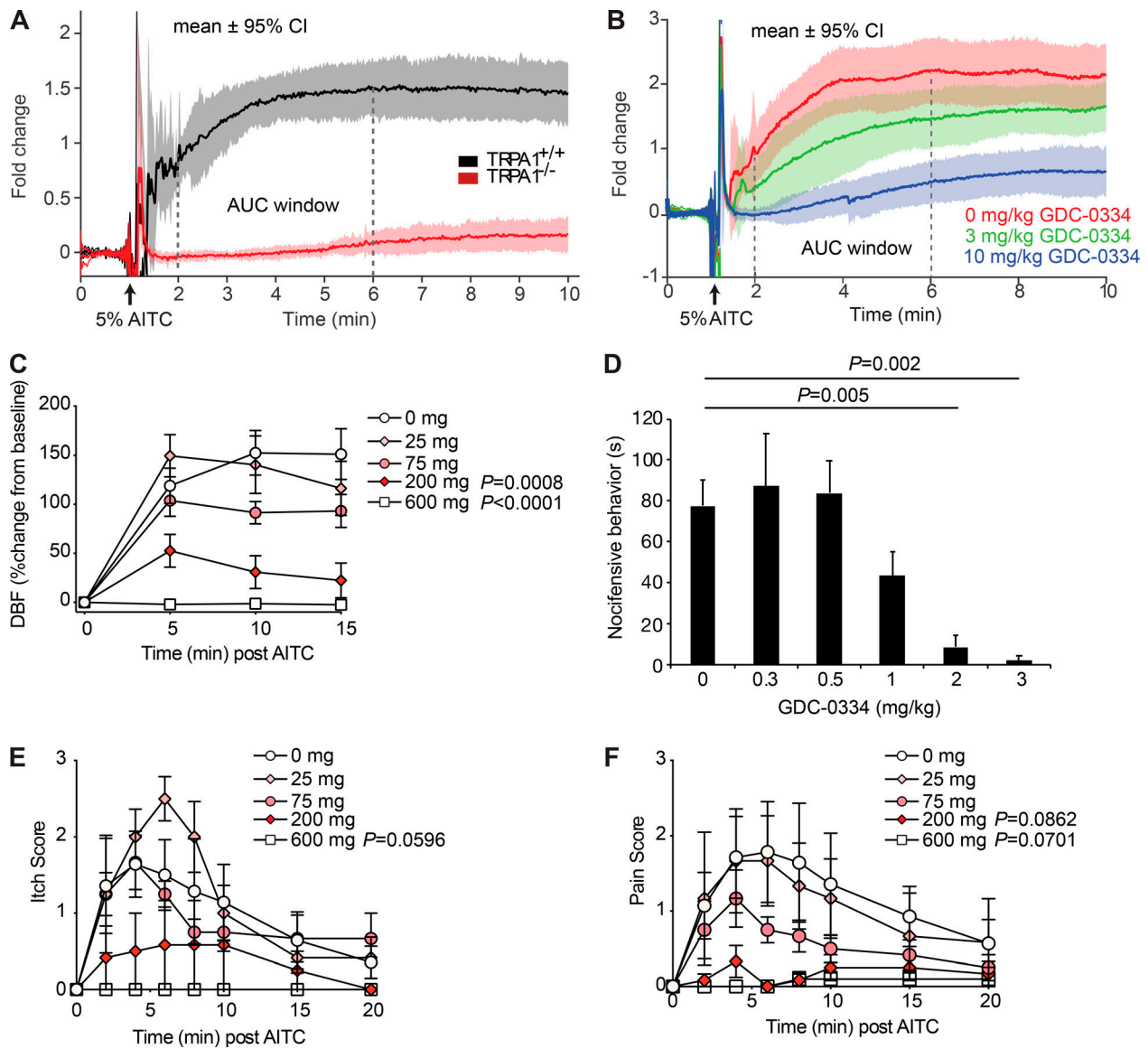


Figure S5. **GDC-0334 reduces AITC-induced perfusion and nocifensive behavior in rats and itch and pain scores in humans.** (A) Time course of flux signals for rats *Trpa1*^{+/+} (black curve) and *Trpa1*^{-/-} (red curve). Arrow indicates the time of AITC treatment. Mean (bold line) ± 95% CI (shaded area); *n* = 6 animals per group. (B) Time course of flux signals for rats dosed with 0 (red), 3 (green), or 10 mg/kg (blue) GDC-0334. Arrow indicates the time of AITC treatment. Mean (bold line) ± 95% confidence interval (CI; shaded area); *n* = 6 animals per group. (C) Time course of mean fold change in the DBF signal relative to baseline following application of 15% AITC for each GDC-0334 dosing human cohort: *n* = 7 (0 mg), 6 (25 mg), 6 (75 mg), 6 (200 mg), and 5 (600 mg); data shown as mean ± SEM; repeated-measures ANOVA was used for statistical analysis. (D) Nocifensive behavior in rats pretreated with indicated doses of GDC-0334. Rats display flinching and hind paw-directed licking and biting (i.e., nocifensive behavior) upon intraplantar injection of AITC that is suppressed by GDC-0334 pretreatment in a dose-dependent manner. Data shown as mean ± SEM; repeated-measures ANOVA was used for statistical analysis. (E and F) Time course of itch (E) and pain (F) scores following topical application of AITC. *n* = 7 (0 mg), 6 (25 mg), 6 (75 mg), 6 (200 mg), and 5 (600 mg). Data are expressed as the mean ± SEM; repeated-measures ANOVA was used for statistical analysis.

Provided online are two tables. Table S1 lists GDC-0334 potency and selectivity. Table S2 presents cryoEM structure statistics.